

Electronic Thesis and Dissertation Repository

---

2-2014 12:00 AM

## Micro-Computed Tomography Semi-Empirical Beam Hardening Correction: Method And Application To Meteorites

David R. Edey  
*The University of Western Ontario*

Supervisor  
Roberta Flemming  
*The University of Western Ontario* Joint Supervisor  
David Holdsworth  
*The University of Western Ontario*

Graduate Program in Geology  
A thesis submitted in partial fulfillment of the requirements for the degree in Master of Science  
© David R. Edey 2014

Follow this and additional works at: <https://ir.lib.uwo.ca/etd>



Part of the [Geology Commons](#)

---

### Recommended Citation

Edey, David R., "Micro-Computed Tomography Semi-Empirical Beam Hardening Correction: Method And Application To Meteorites" (2014). *Electronic Thesis and Dissertation Repository*. 2000.  
<https://ir.lib.uwo.ca/etd/2000>

This Dissertation/Thesis is brought to you for free and open access by Scholarship@Western. It has been accepted for inclusion in Electronic Thesis and Dissertation Repository by an authorized administrator of Scholarship@Western. For more information, please contact [wlsadmin@uwo.ca](mailto:wlsadmin@uwo.ca).

MICRO-COMPUTED TOMOGRAPHY SEMI-EMPIRICAL BEAM HARDENING  
CORRECTION: METHOD AND APPLICATION TO METEORITES

Thesis format: Integrated Article

by

David Ryan Edey

Graduate Program in Geology

A thesis submitted in partial fulfillment  
of the requirements for the degree of  
Master of Science

The School of Graduate and Postdoctoral Studies  
The University of Western Ontario  
London, Ontario, Canada

© David Ryan Edey, 2014

## Abstract

X-ray micro-computed tomography ( $\mu$ CT) is able to non-destructively provide high-resolution 3D images of the internal structures of dense materials such as meteorites. The widespread availability of instruments capable of biomedical micro-computed tomography means there is ample access to scanners for the investigation of geomaterials, but the scan data can be susceptible to artifacts such as beam hardening, a consequence of high X-ray attenuation in these dense materials.

A semi-empirical correction method for beam hardening and scatter that can be straightforwardly applied to available biomedical scanners is proposed and evaluated. This method uses aluminum as a single calibration material to significantly reduce or remove signal intensity errors (i.e. cupping) that occur as a result of beam hardening artifacts. X-ray transmission data are linearized using custom software. Results show that it is possible through careful analysis to determine an effective method of artifact correction for specified protocols using this implementation.

Following correction and validation, this technique is applied to imaging of meteorite samples. Four meteorites are examined using  $\mu$ CT in combination with this processing technique: Three ordinary chondrites (Grimsby, Gao-Guenie, and Ozona) and an olivine diogenite (NWA 5480). Information from  $\mu$ CT is compared to that of traditional methods of analysis of meteoritic samples, and the advantages and disadvantages are discussed.

**Keywords:** computed tomography, attenuation, geomaterials, beam hardening, empirical correction, meteorite, volumetric analysis.

## Acknowledgments

First I would like to thank my supervisors. David, thank you for taking me in and offering your mentorship, wealth of knowledge and resources to allow me to do this research. Robbie, thank you providing both professional and personal support over the many years, countless coffee breaks and much needed beer breaks, thanks for everything.

Phil, you basically become a third supervisor, something you didn't need to do. Thank you for all the professional and person support, ideas, and great games nights.

Thanks to everyone in the Robarts lab, you made my day much less productive and lunch breaks much longer, thanks for that. Much thanks to the crew: Adam P, Chris N, Dan L, Dave M, Hristo N, Ivalio P, Jacques M, Jacques M, Justin T, Kevin B, Kim B, Maria D, Steve P, Zing-Bot.

To Robbie's lab, thanks for listening to me ramble about weird x-ray science and providing much needed feedback. Alex R, Beth D, Jared S, Jeff B, Josh H, Matt I, Mike C, Mike B, Patrick S.

Tim Officer, Laura Sanchez, Jess Stromberg, thanks for being the easiest to convince to go get a beer, the on and off topic discussions, and the late nights.

Simon Deluce and CJ Vitanza thanks for all the support in everything I do, for the advice, ideas, and great times. Thanks for losing at Catan all the time; it made me feel more accomplished even when I wasn't.

Grace, thank you for being yourself and supporting me though this entire process.

To my Brother, Mike, for everything, ever.

To my parents, Myra and Thomas Edey, for without you I wouldn't be here, in every step along the way you have provided me with countless opportunities to do what ever I wanted to.

*The sun, with all those planets revolving around it and dependent on it,  
can still ripen a bunch of grapes as if it had nothing else in the universe  
to do.*

- Galileo Galilei

# Table of Contents

<b>Abstract</b> .....	<b>ii</b>
<b>Acknowledgments</b> .....	<b>iii</b>
<b>Table of Contents</b> .....	<b>v</b>
<b>List of Tables</b> .....	<b>viii</b>
<b>List of Figures</b> .....	<b>ix</b>
<b>Chapter 1</b> .....	<b>1</b>
<b>1 Introduction</b> .....	<b>1</b>
1.1 Meteoritics .....	1
1.2 Micro-Computed Tomography .....	5
1.2.1 Beam Hardening .....	7
1.3 Micro-Computed Tomography of Geomaterials .....	10
1.4 Scope of Thesis .....	11
1.5 References .....	12
<b>Chapter 2</b> .....	<b>15</b>
<b>Co-Authorship Statement</b> .....	<b>15</b>
<b>2 Extended dynamic range micro-computed tomography of geomaterials using a biomedical scanner</b> .....	<b>15</b>
2.1 Introduction.....	15
2.2 Methods.....	17
2.2.1 Theoretical basis of the correction algorithm .....	17
2.2.2 Biomedical micro-CT scanners.....	19
2.2.3 Calibration phantom.....	20
2.2.4 Data analysis .....	21
2.2.4.1 Calibration data .....	24

2.2.4.2	Reconstruction analysis .....	25
2.3	Results.....	25
2.3.1	Calibration data.....	25
2.3.2	Reconstruction analysis .....	27
2.3.2.1	PMMA samples .....	29
2.3.2.2	Aluminum samples.....	32
2.4	Discussion.....	34
2.4.1	GE eXplore speCZT .....	35
2.4.2	GE Locus Ultra .....	36
2.4.3	Summary, limitations, and future work .....	37
2.5	Conclusion .....	41
2.6	References.....	42
<b>Chapter 3</b>	<b>.....</b>	<b>43</b>
<b>Co-Authorship Statement</b>	<b>.....</b>	<b>43</b>
<b>3</b>	<b>Phase recognition and volumetric analysis of meteoritic samples using laboratory micro-computed tomography.....</b>	<b>43</b>
3.1	Introduction.....	43
3.2	Methods.....	46
3.2.1	Equipment and software .....	46
3.2.1.1	LEO 440 SEM .....	46
3.2.1.2	Micro X-Ray diffraction.....	46
3.2.1.3	Biomedical micro-CT scanners .....	47
3.2.1.4	Beam hardening correction.....	47
3.2.1.5	Olympus STM6 measuring microscope .....	48
3.2.2	Sample analysis.....	48
3.2.2.1	MicroView .....	48

3.2.2.2	Point counting.....	48
3.2.3	Selection of meteoritic specimens .....	48
3.3	Results.....	49
3.3.1	Ozona .....	49
3.3.2	Gao-Guenie.....	50
3.3.3	Grimsby.....	54
3.3.4	NWA 5480.....	61
3.4	Discussion.....	67
3.4.1	Ozona .....	67
3.4.2	Gao-Guenie.....	68
3.4.3	Grimsby.....	69
3.4.4	NWA 5480.....	70
3.4.5	Summary, limitations, and future work .....	71
3.5	Conclusion .....	71
3.6	References.....	73
<b>Chapter 4</b>	.....	<b>76</b>
<b>4</b>	<b>Conclusions and Future Directions .....</b>	<b>76</b>
4.1	Summary of Results.....	76
4.2	Future Work.....	78
4.2.1	CT Calibration of Mineralogy .....	78
4.2.2	Dual-Energy CT.....	78
4.2.3	Industrial Scanner Calibration .....	79
4.3	References.....	80
<b>Curriculum Vitae</b>	.....	<b>82</b>



## List of Tables

Table 2.1 - Formulas and coefficients of determination for each fitting parameters.....	25
Table 2.2 - Average and standard deviation of percent cupping in PMMA data described by <i>equation 3</i> , for CT scanners a) speCZT and b) Ultra.....	28
Table 2.3 - Average and standard deviation of percent cupping in aluminum data described by <i>equation 3</i> , for CT scanners a) speCZT and b) Ultra.....	28
Table 2.4 - Volumetric Analysis for Corrected and Uncorrected Gao Guenie Sample.....	40
Table 3.1 - Volumetric Analysis of Ozona .....	50
Table 3.2 - Volumetric Analysis of Gao-Guenie .....	54
Table 3.3 - Volumetric Analysis of Grimsby.....	58
Table 3.4 - Mineral Phases in NWA 5480 by $\mu$ XRD .....	63
Table 3.5 - Volumetric Analysis of NWA 5480 .....	64

## List of Figures

Figure 1.1 - Diagram expressing the systematics of meteorite classification. Showing the major meteorite divisions. (Weisberg et al., 2006).....	4
Figure 1.2 - GE eXplore speCZT. Located at the Robarts Research Institute, this scanner was utilized for both testing of beam hardening correction as well as collection of volumetric meteoritic data.....	6
Figure 1.3 - Cone beam CT scanning configuration. To provide multiple projection angles, the sample or the source and detector are rotated around an axis (adapted from <a href="http://serc.carleton.edu/research_education/geochemsheets/techniques/CT.html">http://serc.carleton.edu/research_education/geochemsheets/techniques/CT.html</a> ) .....	7
Figure 1.4 - Idealized X-ray tube spectrum. X-ray spectrum prior to and after filtration through 1.3 cm of aluminium.....	8
Figure 1.5 – Artifacts in CT caused by hardening of the beam. a) cupping, or artificially lower density reported in the center of a homogeneous rod of aluminum, and b) streaking, or artificially high and low density <i>streaks</i> reported between two objects with significantly higher density than their surrounding. ....	9
Figure 2.1 - Plot of transmission vs. thickness for aluminum calibrator. CT scans of the aluminium calibrator were completed on the speCZT at 90 kVp and 40 mA. This plot shows the non-linearity of thickness to transmission ratio of photons. The straight line represents the expected linear response. ....	18
Figure 2.2 - Calibration phantoms for beam hardening correction in CT. Phantoms were fabricated from a) PMMA and b) Aluminum by gluing disks of various diameters to each other in an alternating fashion. Scale cube (1 cm) for size reference. ....	21
Figure 2.3 - Transmission images of CT calibration phantoms. Scans were performed on both a) PMMA and b) aluminum calibration phantoms using the speCZT scanner at 90 kVp and 40 mA. Images from the Ultra scanner (which appear the same) were used for corresponding calibration. ....	22

Figure 2.4 - Locations of the ROI measurements used for percent cupping analysis. Nine ROI measurements, here shown on 63.5 mm rod, from selected CT scan planes were taken on each testing rod. Four measurements were taken in the edges of the object, four in the surrounding air and one in the center of the object..... 24

Figure 2.5 - Plots of transmission ratio vs. thickness of calibration phantoms in speCZT scanner. CT scan data of both calibration phantoms acquired from speCZT (90 kVp, 40 mA) were used to construct transmission ratio vs. thickness plots of the PMMA calibrator data with a) polynomial fit, b) one-phase inverse decay fit, and aluminum calibrator data with c) polynomial fit and d) one-phase inverse decay fit..... 26

Figure 2.6 - Plots of transmission ratio vs. thickness of calibration phantoms in Ultra scanner. CT scan data of both calibration phantoms acquired from Ultra (120 kVp, 20 mA) were used to construct transmission ratio vs. thickness plots of the PMMA calibrator data with a) polynomial fit, b) one-phase inverse decay fit, and aluminum calibrator data with c) polynomial fit and d) one-phase inverse decay fit..... 27

Figure 2.7 - Correction of 63.5 mm PMMA rod scanned on speCZT with image and line profile. CT scan planes and corresponding line profiles of a 63.5 mm PMMA rod scanned on the speCZT (90 kVp, 40 mA) following a) no correction, and correction methods as obtained from the PMMA calibrator using b) polynomial fit, c) one-phase inverse decay fit, and the aluminum calibrator using d) polynomial fit and e) one-phase inverse decay fit..... 30

Figure 2.8 - Correction of 63.5 mm PMMA rod scanned on Ultra with image and line profile. CT scan planes and corresponding line profiles of a 63.5 mm PMMA rod scanned on the Ultra (120 kVp, 20 mA) following a) no correction, and correction methods as obtained from the PMMA calibrator using b) polynomial fit, c) one-phase inverse decay fit, and the aluminum calibrator using d) polynomial fit and e) one-phase inverse decay fit..... 31

Figure 2.9 - Correction of 38.1 mm aluminum rod scanned on speCZT with image and line profile. CT scan planes and corresponding line profiles of a 38.1 mm aluminum rod scanned on the speCZT (90 kVp, 40 mA) following a) no correction, and correction methods as obtained from the aluminum calibrator using b) polynomial fit and c) one-phase inverse decay fit..... 33

Figure 2.10 - Correction of 50.8 mm aluminum rod scanned on Ultra with image and line profile. CT scan planes and corresponding line profiles of a 50.8 mm aluminum rod scanned on the Ultra (120 kVp, 20 mA) following a) no correction, and correction methods as obtained from the aluminum calibrator using b) polynomial fit and c) one-phase inverse decay fit.....	34
Figure 2.11 - Correction of 50.8 mm aluminum rod scanned on speCZT with image and line profile. CT scan planes and corresponding line profiles of a 50.8 mm aluminum rod scanned on the speCZT (90 kVp, 40 mA) following a) no correction, and correction methods as obtained from the aluminum calibrator using b) polynomial fit and c) one-phase inverse decay fit. In this scan, the parameters used on the speCZT did not provide enough flux. ....	36
Figure 2.12 – Pre and Post-Correction of Gao Guenie with line profile. Gao Guenie and associated line profile a) uncorrected and b) corrected with aluminium one-phase decay correction. Bright spots indicate material of high radiodensity, mainly kamacite and taenite, surrounded by the silicate bulk material. ....	40
Figure 3.1 - Photo of Ozona. Scale cube (1 cm) for size reference. ....	50
Figure 3.2 – Photo vs CT scan of Ozona. a) A photomicrograph, obtained using a standard office scanner and b) a CT slice through the surface collected on the speCZT at 110 kVp and 40 mA.....	51
Figure 3.3 – CT slices through Ozona. CT slices through Ozona every 1.3 mm, beginning 650 $\mu$ m below surface collected on the speCZT at 110 kVp and 40 mA. ....	52
Figure 3.4 - Photo of Gao-Guenie. Scale cube (1 cm) for size reference. ....	53
Figure 3.5 - CT vs. Photo, including point counting grid of Gao-Guenie. a) photomicrograph overlain with a point counting grid and results (red = non-metallic; blue = metallic) b) the original photomicrograph obtained using an Olympus STM 30, and c) a CT slice through the surface collected on the speCZT at 110 kVp and 40 mA. ....	53
Figure 3.6 - CT slices through Gao-Guenie. CT slices through Gao-Guenie every 1.4 mm, beginning 700 $\mu$ m below surface collected on the speCZT at 110 kVp and 40 mA. ....	54

Figure 3.7 - Photo of Grimsby samples. Three Grimsby samples a) HP-2, b) Zbyszek and c) Peter. Scale cube (1 cm) for size reference.....	55
Figure 3.8 – SEM, EDX and CT images of Grimsby sample HP-2. a) SEM image of the surface, b) CT slices though the surface collected on the Locus at 80 kVp and 0.45 mA and EDX elemental maps of the surface (below) of Grimsby sample HP-2.....	56
Figure 3.9 - SEM, EDX and CT images of Grimsby sample Zbyszek. a) SEM image of the surface, b) CT slices though the surface collected on the Locus at 80 kVp and 0.45 mA and EDX elemental maps of the surface (below) of Grimsby sample Zbyszek.....	57
Figure 3.10 - SEM, EDX and CT images of Grimsby sample Peter. a) SEM image of the surface, b) CT slices though the surface collected on the Locus at 80 kVp and 0.45 mA and EDX elemental maps of the surface (below) of Grimsby sample Peter.....	58
Figure 3.11 - CT slices through Grimsby sample HP-2. CT slices thought Grimsby sample HP-2 every 200 $\mu\text{m}$ starting 100 $\mu\text{m}$ below surface collected on the Locus at 80 kVp and 0.45 mA.....	59
Figure 3.12 - CT slices through Grimsby sample Zbyszek. CT slices thought Grimsby sample Zbyszek every 200 $\mu\text{m}$ starting 100 $\mu\text{m}$ below surface collected on the Locus at 80 kVp and 0.45 mA.....	60
Figure 3.13 - CT slices through Grimsby sample Peter. CT slices thought Grimsby sample Peter every 200 $\mu\text{m}$ starting 100 $\mu\text{m}$ below surface collected on the Locus at 80 kVp and 0.45 mA.....	61
Figure 3.14 - Photo of NWA 5480. A coarse-grained olivine diogenite. Scale cube (1 cm) for size reference.....	62
Figure 3.15 - Photo vs. CT scan, including $\mu\text{XRD}$ locations on NWA 5480. a) photomicrograph, obtained using a standard office scanner, indicating locations that $\mu\text{XRD}$ were performed, and b) a CT slice through the surface collected on the speCZT at 110 kVp and 40 mA.....	63

Figure 3.16 - $\mu$ XRD Diffraction pattern at locations 1 and 2. Diffraction pattern obtained at both locations 1 and 2 with a International Centre for Diffraction Data (ICDD) stick pattern for chromite, indicating diffraction match found.....	64
Figure 3.17 - $\mu$ XRD Diffraction pattern at locations 3 and 6 - 10. Diffraction pattern obtained at both locations 3 and 6 - 10 with a ICDD stick pattern for enstatite, indicating diffraction match found.....	65
Figure 3.18 - $\mu$ XRD Diffraction pattern at locations 4 and 5. Diffraction pattern obtained at both locations 4 and 5 with a ICDD stick pattern for forsterite, indicating diffraction match found. ....	66
Figure 3.19 - CT slices though NWA 5480. CT slices thought NWA 5480 every 1.50 mm starting 0.75 mm below surface collected on the speCZT at 110 kVp and 40 mA. ....	67

## Chapter 1

### 1 Introduction

Humanity's fascination with the night sky predates recorded history. For as long as we have existed, humans have looked into the sky and wondered what stories it could tell. From the early study of the skies we began to understand the length of a year, and began to be able to predict the seasons, knowing when to plant crops for the best harvests, giving us a better understanding of the cyclic system that our world is going through. As we established our scientific systems, and our technology to study our solar system developed, it became more obvious that there was more out there than we initially thought. The cosmos was more than just ether, holding the stars in place, or spheres rotating inside of each other allowing all the celestial bodies to move amongst each other. We began to understand that the Earth was not the center of the universe, nor the center of our solar system for that matter. There was much, much more to the story.

Meteorites themselves have been heralded throughout human history, even from before we had any knowledge of what they really were or where they came from, often believing that they were gifts from God or had lost their hold in the celestial ether (McSween, 1999). Humans have had a longstanding fascination with these *thunder stones*.

#### 1.1 Meteoritics

This fascination with the night sky has turned into multifaceted research studying much of universe outside our own world. We have gained enough knowledge to not only study the environment of our solar system from our home world but we have amassed many hours of human spaceflight, space walks, and maintain permanent residence in orbit around Earth since the 2<sup>nd</sup> of November, 2000; without the study of our planet this would never have been possible. One major facet in the study of planetary science is the study of meteoritics: the study of meteors, meteorites, and other extraterrestrial materials.

Meteorites' various compositions suggest that they have had various origins. Meteorites that have been ejected from other solar system bodies contain information about their

parent bodies, and have provided insight into their geology and composition. These samples often have undergone some level of alteration providing insight into the geological processes that have occurred on their parent body, from bombardment to aqueous and thermal metamorphism (McSween & Huss, 2010). Understanding the minerals and other phases within these meteorites can help us develop more comprehensive models of these systems. Some meteorites, however, have remained mostly unaltered since the time of their formation. These meteorites, containing chondrules, and sometimes calcium aluminum inclusions (CAIs), two of the oldest solid materials from the formation of our solar system, help us better understand the processes that occur during the initial cooling of our protoplanetary disk (Brearley & Jones, 1998). There are, of course, bodies in our solar system that are at every stage between these two extremes. Meteorites that stem from these locations give us information about the history of our solar system. Dating methods allow scientists to arrange these meteorites in chronological order from which we have begun to develop an understanding of the order in which events happened in the formation of our, and possibly other, solar systems (Mittlefehldt et al., 1998).

Meteorites fall into one of several categories. Most meteorites are chondrites, making up 85% of the observed falls (Weisberg et al., 2006). Chondrites are primitive rocks that are physical mixtures of characterizable mineralogies, having bulk elemental compositions similar to the Sun. These meteorites contain chondrules and CAIs, the initial solid materials to form during the cooling of our solar system. The other 15% of meteorites by observed falls consist of differentiated materials; much like Earth (although in a much smaller scale) they have undergone melting and recrystallization, separating the primitive silicate and metallic constituents. These processes destroy the chondrules they once contained and produce achondritic meteorites, which are subdivided into three types: irons, stony irons, and silicate meteorites from the mantle and crust of other bodies (such as martian and lunar meteorites) that have undergone differentiation. Primitive achondrites are the solid residues left behind by partial melting of the chondritic material whereas magmatic achondrites have completely melted and become highly differentiated. Irons and stony iron meteorites are formed when metals and sulphides are



separated from molten silicates (*Figure 1.1*) (McSween & Huss, 2010; Weisberg et al., 2006).

There is much to be learned from these *space rocks* that conveniently get delivered to our home planet on a regular basis, but how do we glean the maximum amount of information from these samples? There are a vast array of methods to study these samples, from traditional petrographic analysis of thin sections by optical microscopy (Brearley & Jones, 1998), electron probe EDX/SEM (Hashimoto & Grossman, 1985; Herd et al., 2010; Merouane et al., 2011) to Rietveld refinement of powder X-ray diffraction data (Cloutis et al., 2013; Izawa, Flemming, et al., 2010; Izawa, King, et al., 2010). Unfortunately these methods require some amount of alteration to the sample to provide analysis, e.g. cutting, powdering or exposure to epoxy and coating agents. All destructive techniques reduce the future analysis capabilities of these samples, which are only few in number and therefore of high scientific value.

Fortunately, the development of X-ray micro-computed tomography during the past several years has allowed us, for the first time, to image the inside of these samples, providing volumetric information about the interior of meteorites in a non-destructive manner, allowing for scientific study of these samples without alteration.

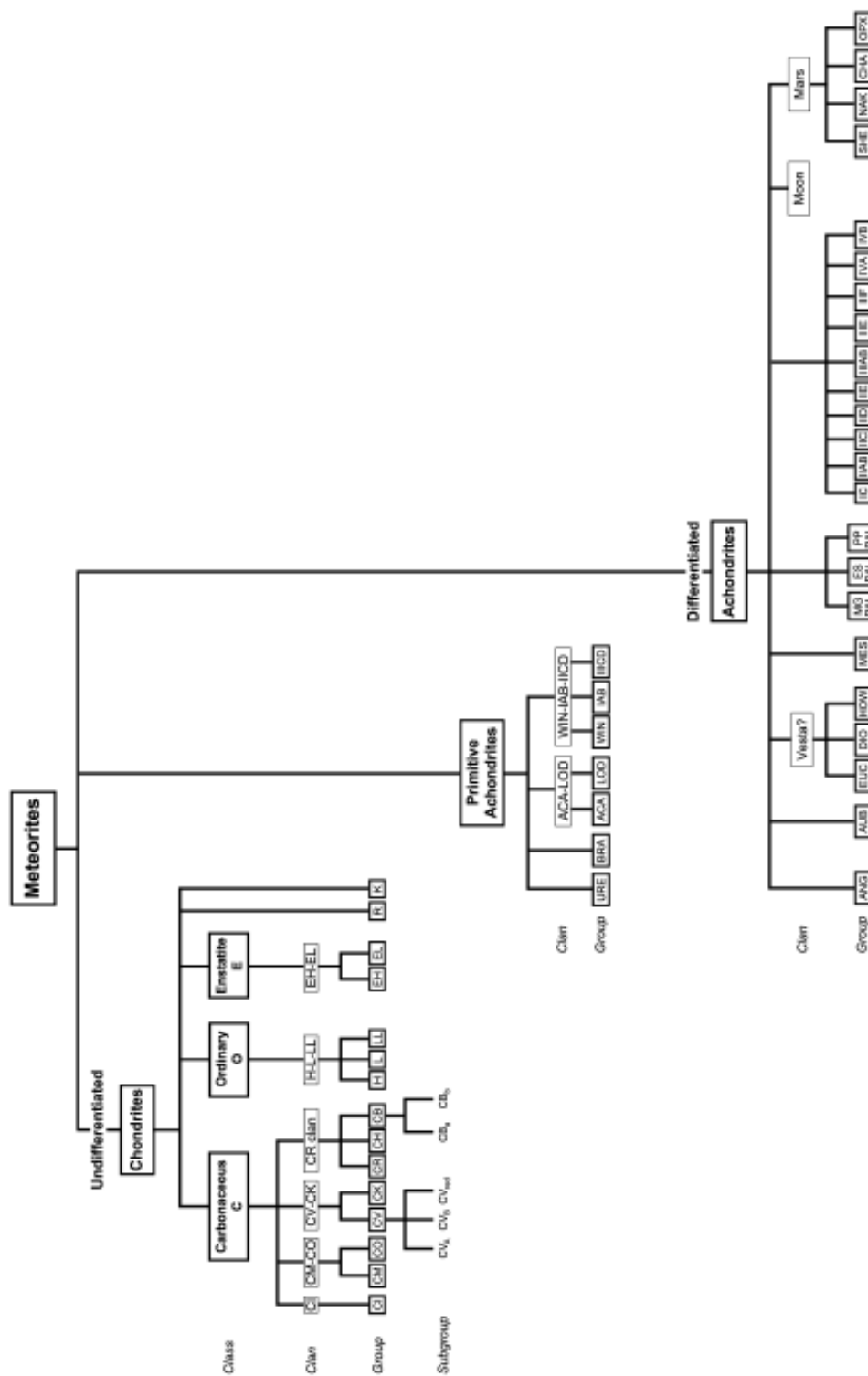


Figure 1.1 - Diagram expressing the systematics of meteorite classification. Showing the major meteorite divisions. (Weisberg et al., 2006)

## 1.2 Micro-Computed Tomography

In its most basic sense, X-ray computed tomography is a process of collecting a series of total X-ray attenuations through an object along paths of known geometry and using these data to reconstruct images of the interior these objects, allowing the user to non-destructively “see” the inside. The image that is produced consists of a 3D array of volume elements (i.e. voxels, or 3D pixels) that represent the radiodensity, or linear X-ray attenuation, of the material contained within each voxel.

Modern micro-CT machines (e.g. the GE eXplore speCZT located at the Robarts Research Institute, *Figure 1.2*) are constructed using cone-beam X-ray sources and 2D X-ray detectors (*Figure 1.3*), allowing for multiple paths of attenuation to be collected simultaneously. Most modern CT machines, and the three discussed in this thesis, utilize a gantry system that allows the X-ray source and detector to rotate around the specimen, collecting hundreds of separate 2D X-ray projections at multiple angles in a relatively short time. The duration of the collection of projections relies on the amount of photons being produced by the X-ray source, the efficiency of the X-ray detector, and the amount of attenuation of the photons by the scanned material. This is analogous to taking a picture, where the shutter time required to collect a properly exposed photo depends on the amount of light hitting the subject, the detector sensitivity (i.e. ISO) and the amount of light that is being reflected off the subject towards the camera. It is possible to make trade-offs in the system to collect scans faster or slower while impacting the image quality, just as it is possible to take a picture in low light at a quick speed at the cost of producing an under exposed or noisy image. It is possible to saturate the detectors or produce no photons on the detector surface, reducing or removing contrast, therefore careful selection of the scanning parameters is integral into collecting a properly exposed image. After collection of a series of 2D images it is necessary to reconstruct the 3D volume. The 2D images are convolved to reduce blur and then back-projected into the 3D space to create the final image.



**Figure 1.2 - GE eXplore speCZT.** Located at the Robarts Research Institute, this scanner was utilized for both testing of beam hardening correction as well as collection of volumetric meteoritic data.

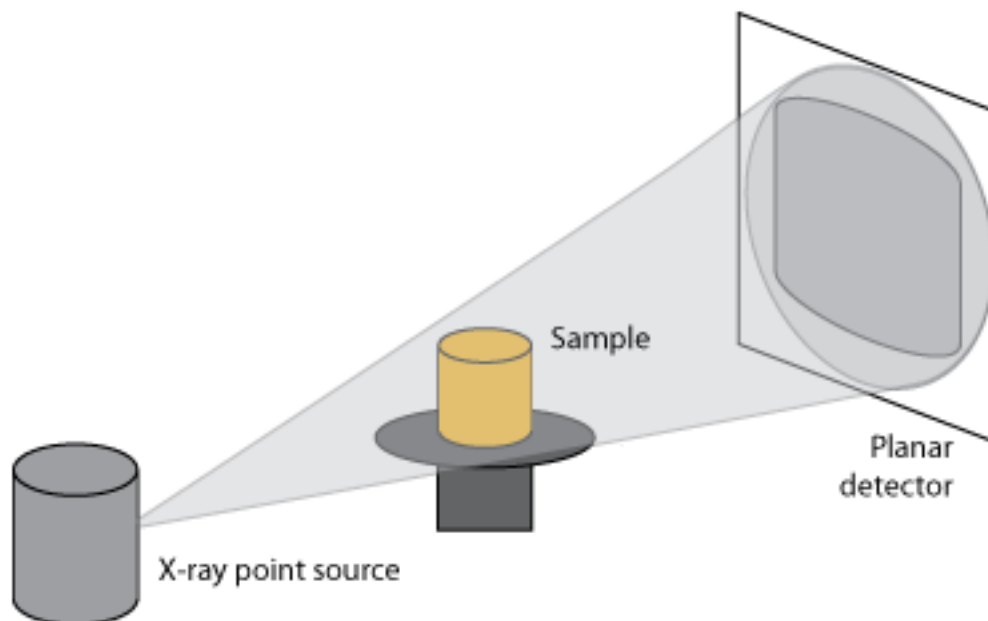


**Figure 1.3 - Cone beam CT scanning configuration.** To provide multiple projection angles, the sample or the source and detector are rotated around an axis  
(adapted from [http://serc.carleton.edu/research\\_education/geochemsheets/techniques/CT.html](http://serc.carleton.edu/research_education/geochemsheets/techniques/CT.html))

Micro-Computed Tomography ( $\mu$ CT) functions in the same manner as clinical CT scanners, but provides higher reconstruction resolution. Additionally,  $\mu$ CT machines are usually constructed to produce images with isotropic voxels, allowing resolution to remain the same in all reconstruction planes. This is achieved by smaller detector pixels, more focused X-ray sources, and a higher dose of photons being produced.

### 1.2.1 Beam Hardening

The X-ray tubes utilized in radiography, including CT, produce a spectrum of photons at various energies. The energy of the spectrum is denoted by the peak energy of the spectrum, so a spectrum ranging from 20 – 120 keV would be labeled as 120 peak electron kilovoltage (120 kVp). All materials preferentially absorb lower energy photons in the spectrum, mostly through photoelectric absorption (Grodstein, 1957), causing the remaining spectrum to be proportionally richer in high energy photons. This causes the resulting X-ray spectrum to become more penetrating and thus “harder”. As seen in

Figure 1.4, the result of filtering a idealized X-ray source's spectrum through 1.3 cm of aluminum is not only a reduction in photon fluence across the spectrum, but also an increased mean energy (from 51.3 to 58.7 keV, in this case).

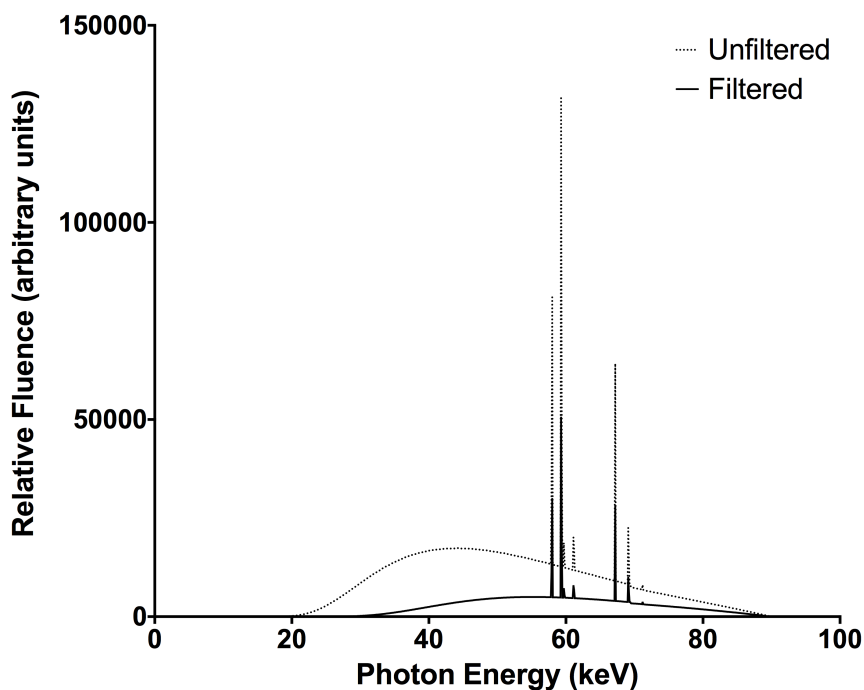


**Figure 1.4 - Idealized X-ray tube spectrum.** X-ray spectrum prior to and after filtration through 1.3 cm of aluminium.

The attenuation of a homogeneous material is not strictly proportional to its thickness; the Beer-Lambert law does not apply to a polyenergetic source. As a result, the gray-scale values given on the individual radiographs are not a sum of the linear attenuations, as assumed during reconstruction (Van de Casteele et al., 2002). This effect produces artifacts in the reconstruction volume such as the centers of objects being reported at lower radiodensities than the edges (referred to as *cupping*) and streaking between two objects of high density into a surrounding that is significantly lower density (Figure 1.5) (Brooks & Di Chiro, 1976; Chen et al., 2001). Note that a monochromatic source would not exhibit these artifacts (Herman, 1979). Beam hardening is more pronounced in objects of higher X-ray attenuation, as these materials are able to harden the beam over shorter ray paths, exacerbating the issue.

As a result of the artificially low values that are reported in the centers of objects, streaking occurs (Barrett & Keat, 2004). This is a result of the reconstruction algorithm requiring self-consistency. The objects are reporting to be of lower density, resulting in the total attenuation along the paths not adding to the full attenuation observed; the material between the two objects must be assigned a higher density in the reconstruction, resulting in streaking.

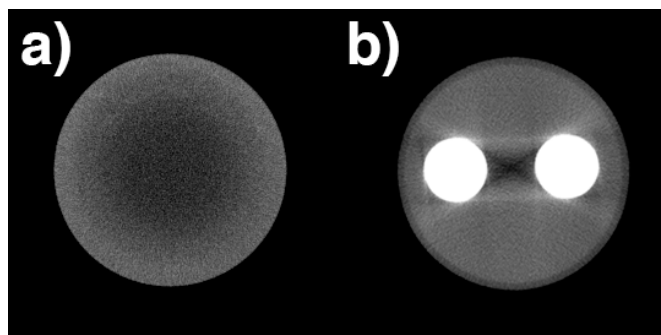


**Figure 1.5 – Artifacts in CT caused by hardening of the beam.** a) cupping, or artificially lower density reported in the center of a homogeneous rod of aluminum, and b) streaking, or artificially high and low density *streaks* reported between two objects with significantly higher density than their surrounding.

The hardening of the X-ray spectrum occurs more predominately in  $\mu$ CT systems with lower mean energies. Industrial scanners that have more energetic X-ray spectra ( $> 200$  kVp) are less likely to exhibit this artifact. Medical X-ray tomography machines are constructed with X-ray sources that produce lower energy spectra, providing higher contrast in material with low attenuation and critically reducing the X-ray dose to subjects (animal or otherwise). While the number of biomedical  $\mu$ CT scanners outnumbers those built for industrial applications, they are more susceptible to beam hardening artifacts.

Traditionally, during the initial development of X-ray CT, one would be required to surround the part of the body attempting to be scanned in a water bath, this would provide similar path lengths and attenuations to all of the beam paths, reducing the observed cupping due to beam hardening (Brooks & Di Chiro, 1976). One method for

reducing cupping without the need for a water path is to apply a filter between the X-ray source and detector, effectively *prehardening* the beam (Ketcham & Carlson, 2001; Ritman, 2004). This is an effective way of reducing the hardening that occurs through the object, as the beam has already become more penetrating, but reduces the total photons and therefore increases scanning time to produce images of similar quality to those without filtering. Additionally, the more penetrating beam causes contrast in the reconstruction volume to be reduced (Van de Casteele et al., 2002).

### 1.3 Micro-Computed Tomography of Geomaterials

There have been significant developments in the application of quantitative CT and micro-CT to geomaterials. Current studies have used various forms of CT to provide textural analysis of metamorphic rocks (Denison et al., 1997), determining flow patterns in soils non-destructively (Heijs et al., 1995; Heijs et al., 1996), examining the quality of cataclastic carbonate samples (Christe et al., 2011), correlating the microstructure and permeability of saturated bentonites (Kawaragi et al., 2009) and determining soil pore characteristics (Munkholm et al., 2012). The non-destructive aspect of CT has also proved itself invaluable in the analysis of one-of-a-kind items such as Archaeopteryx fossils (Haubitz et al., 1988). Advanced medical imaging techniques such as dual-energy CT have also been applied to geological sampling (Iovea et al., 2009).

The use of CT imaging in the geosciences and meteoritics is developing at an increasing pace; however, most geologists and meteoriticists still don't understand the potential of this imaging technique (Mees et al., 2003), and because of the misunderstanding of application of the much more readily available bio-medical scanners most of these studies are performed on higher energy, industrial CT machines (Benedix et al., 2008), or even more so on synchrotron CT (Ebel & Rivers, 2007; Ebel et al., 2008; Friedrich et al., 2008; Hirano et al., 1990). The research described in this thesis addresses the opportunities for non-destructive analysis of geological and meteoritic material with existing biomedical micro-CT scanners.



## 1.4 Scope of Thesis

In this thesis I attempt to correct for micro-CT intensity artifacts by collecting attenuation calibration data across a variety of known thicknesses for a homogeneous material with an X-ray attenuation that approximates meteorites and most other geomaterials. Using this empirical data and modeling the non-linear response of the system on the collected projection data (prior to reconstruction), I propose that it is possible to re-linearize the data and reduce or remove the offending artifacts. This has the benefit of working using the same scan parameters as already used on the system, and provides the ability to post-correct scans that have been previously collected, provided that the original projection data have been preserved. The ability to correct for these artifacts is an important step in the quantitative analysis of meteorites and all geomaterials when scanned on a biomedical scanner. Without correction there will not be a uniform density across samples, resulting in improper segmentation though radiodensity for volumetric analysis as well as confounded qualitative analysis due to cupping, and streak artifacts obscuring detail in the volumes.

The overall scope of this thesis is to provide a method that can accurately provide volumetric analysis of the mineralogy within meteoritic samples. This challenge can be broken into two major objectives, divided into the two following chapters:

1. Produce and validate a correction for beam hardening in X-ray computed tomography methodology that will significantly reduce the resulting artifacts.
2. Apply this correction method to meteoritic samples and validate the ability to provide volumetric analysis of the mineralogy within these samples using CT in a way that is advantageous and beneficial to geoscientists.

## 1.5 References

- Barrett, J.F., & Keat, N. (2004). Artifacts in CT: Recognition and avoidance. *Radiographics*, *24*(6), 1679-1691.
- Benedix, G., Ketcham, R., Wilson, L., McCoy, T., Bogard, D., Garrison, D., . . . Middleton, R. (2008). The formation and chronology of the PAT 91501 impact-melt L chondrite with vesicle-metal-sulfide assemblages. *Geochimica et Cosmochimica Acta*, *72*(9), 2417-2428.
- Brearley, A.J., & Jones, R.H. (1998). Chondritic meteorites. *Reviews in Mineralogy and Geochemistry*, *36*(1), 3.1-3.398.
- Brooks, R.A., & Di Chiro, G. (1976). Beam hardening in x-ray reconstructive tomography. *Phys Med Biol*, *21*(3), 390-398.
- Chen, C.Y., Chuang, K.S., Wu, J., Lin, H.R., & Li, M.J. (2001). Beam Hardening Correction for Computed Tomography Images Using a Postreconstruction Method and Equivalent Tissue Concept. *Journal of Digital Imaging*, *14*(2), 54-61.
- Christe, P., Turberg, P., Labiouse, V., Meuli, R., & Parriaux, A. (2011). An X-ray computed tomography-based index to characterize the quality of cataclastic carbonate rock samples. *Engineering Geology*, *117*(3-4), 180-188. doi: 10.1016/j.enggeo.2010.10.016
- Cloutis, E., Izawa, M., Pompilio, L., Reddy, V., Hiesinger, H., Nathues, A., . . . Bell III, J. (2013). Spectral reflectance properties of HED meteorites+ CM2 carbonaceous chondrites: Comparison to HED grain size and compositional variations and implications for the nature of low-albedo features on Asteroid 4 Vesta. *Icarus*.
- Denison, C., Carlson, W.D., & Ketcham, R.A. (1997). Three-dimensional quantitative textural analysis of metamorphic rocks using high-resolution computed X-ray tomography: Part I. Methods and techniques. *Journal of metamorphic geology*, *15*(1), 29.
- Ebel, D.S., & Rivers, M.L. (2007). Meteorite 3-D synchrotron microtomography: Methods and applications. *Meteoritics & Planetary Science*, *42*(9), 1627-1646.
- Ebel, D.S., Weisberg, M.K., Hertz, J., & Campbell, A.J. (2008). Shape, metal abundance, chemistry, and origin of chondrules in the Renazzo (CR) chondrite. *Meteoritics & Planetary Science*, *43*(10), 1725-1740.
- Friedrich, J.M., Wignarajah, D.P., Chaudhary, S., Rivers, M.L., Nehru, C., & Ebel, D.S. (2008). Three-dimensional petrography of metal phases in equilibrated L chondrites—Effects of shock loading and dynamic compaction. *Earth and Planetary Science Letters*, *275*(1), 172-180.

- Grodstein, G.W. (1957). X-ray attenuation coefficients from 10 keV to 100 MeV: DTIC Document.
- Hashimoto, A., & Grossman, L. (1985). *SEM-petrography of Allende fine-grained inclusions*. Paper presented at the Lunar and Planetary Institute Science Conference Abstracts.
- Haubitz, B., Prokop, M., Dohring, W., Ostrom, J.H., & Wellnhofer, P. (1988). Computed Tomography of Archaeopteryx. *Paleobiology*, *14*(2), 206-213.
- Heijs, A.W.J., de Lange, J., Schoute, J.F.T., & Bouma, J. (1995). Computed tomography as a tool for non-destructive analysis of flow patterns in macroporous clay soils. *Geoderma*, *64*(3-4), 183-196. doi: 10.1016/0016-7061(94)00020-b
- Heijs, A.W.J., Ritsema, C.J., & Dekker, L.W. (1996). Three-dimensional visualization of preferential flow patterns in two soils. *Geoderma*, *70*(2-4), 101-116. doi: 10.1016/0016-7061(95)00076-3
- Herd, C., Stern, R., Walton, E., Li, J., & Bibby, C. (2010). *TEM and SEM-CL analysis of baddeleyite in NWA 3171: Geochronological implications for Martian meteorites*. Paper presented at the Lunar and Planetary Institute Science Conference Abstracts.
- Herman, G.T. (1979). Correction for beam hardening in computed tomography. *Phys Med Biol*, *24*(1), 81.
- Hirano, T., Funaki, M., Nagata, T., Taguchi, I., Hamada, H., Usami, K., & Hayakawa, K. (1990). *Observation of Allende and Antarctic meteorites by monochromatic X-ray CT based on synchrotron radiation*. Paper presented at the Proceedings of the NIPR Symposium on Antarctic meteorites.
- Iovea, M., Oaie, G., Ricman, C., Mateiasi, G., Neagu, M., Szobotka, S., & Dului, O.G. (2009). Dual-energy X-ray computer axial tomography and digital radiography investigation of cores and other objects of geological interest. *Engineering Geology*, *103*(3-4), 119-126. doi: 10.1016/j.enggeo.2008.06.018
- Izawa, M., Flemming, R.L., King, P.L., Peterson, R.C., & McCausland, P.J. (2010). Mineralogical and spectroscopic investigation of the Tagish Lake carbonaceous chondrite by X-ray diffraction and infrared reflectance spectroscopy. *Meteoritics & Planetary Science*, *45*(4), 675-698.
- Izawa, M., King, P., Flemming, R., Peterson, R., & McCausland, P. (2010). Mineralogical and spectroscopic investigation of enstatite chondrites by X-ray diffraction and infrared reflectance spectroscopy. *Journal of Geophysical Research: Planets (1991-2012)*, *115*(E7).

- Kawaragi, C., Yoneda, T., Sato, T., & Kaneko, K. (2009). Microstructure of saturated bentonites characterized by X-ray CT observations. *Engineering Geology*, *106*(1-2), 51-57. doi: 10.1016/j.enggeo.2009.02.013
- Ketcham, R.A., & Carlson, W.D. (2001). Acquisition, optimization and interpretation of X-ray computed tomographic imagery: applications to the geosciences. *Comput. Geosci.*, *27*(4), 381-400. doi: 10.1016/s0098-3004(00)00116-3
- McSween, H.Y. (1999). *Meteorites and their parent planets*: Cambridge University Press.
- McSween, H.Y., & Huss, G.R. (2010). *Cosmochemistry*: Cambridge University Press.
- Mees, F., Swennen, R., Van Geet, M., & Jacobs, P. (2003). Applications of X-ray computed tomography in the geosciences. *Geological Society, London, Special Publications*, *215*(1), 1-6.
- Merouane, S., Djouadi, Z., Brunetto, R., Borg, J., & Dumas, P. (2011). *Analyses of a few fragments from the Paris meteorite through SEM/EDX, micro-FTIR and micro-Raman spectroscopies*. Paper presented at the EPSC-DPS Joint Meeting 2011.
- Mittlefehldt, D.W., McCoy, T.J., Goodrich, C.A., & Kracher, A. (1998). Non-chondritic meteorites from asteroidal bodies. *Reviews in Mineralogy and Geochemistry*, *36*(1), 4.1-4.195.
- Munkholm, L.J., Heck, R.J., & Deen, B. (2012). Soil pore characteristics assessed from X-ray micro-CT derived images and correlations to soil friability. *Geoderma*, *181-182*, 22-29. doi: 10.1016/j.geoderma.2012.02.024
- Ritman, E.L. (2004). Micro-computed tomography-current status and developments. *Annu. Rev. Biomed. Eng.*, *6*, 185-208.
- Van de Casteele, E., Van Dyck, D., Sijbers, J., & Raman, E. (2002). An energy-based beam hardening model in tomography. *Physics in medicine and biology*, *47*(23), 4181.
- Weisberg, M.K., McCoy, T.J., & Krot, A.N. (2006). Systematics and evaluation of meteorite classification. *Meteorites and the early solar system II*, *1*, 19-52.

## Chapter 2

### Co-Authorship Statement

Chapter 2 is an original manuscript that is in preparation for submission to the journal *Engineering Geology*, entitled “Extended dynamic range micro-computed tomography of geomaterials using a biomedical scanner.” The manuscript is co-authored by David R. Edey, Steven I. Pollmann, Daniel Lorusso, Maria Draganova, Roberta L. Flemming, and David W. Holdsworth. In my role as a M.Sc. candidate, I participated in designing the study, acquired the images, analyzed all data, performed the statistical analysis, and wrote the manuscript text. Steven Pollmann contributed key technical aspects of the methods, and provided editorial input. Daniel Lorusso aided in the analysis of statistical data provided editorial input. Maria Dranganova and David Holdsworth designed the study. Roberta Flemming and David Holdsworth, as my supervisors, reviewed the results, gave editorial assistance and provided mentorship.

## 2 Extended dynamic range micro-computed tomography of geomaterials using a biomedical scanner

### 2.1 Introduction

With recent hardware advances in micro-computed tomography (micro-CT), non-destructive CT analysis can be implemented on previously incompatible geomaterials such as meteorites, core samples, minerals, and soil samples. These micro-CT advances can also provide speed and archival advantages over destructive methods. However, micro-CT can suffer from dynamic range-limiting artifacts that can obscure detail and limit quantitative and qualitative analysis. Micro-CT imaging can provide ample resolution for many traditional qualitative analysis methods, as well as additional qualitative analysis. The non-destructive nature of micro-CT is especially advantageous for use with specimens that cannot be sectioned. Those specimens of particular interest to the geoscientist include: rare samples in both private and museum collections; samples where destruction would inhibit future research (soil pycnometry, pycnometry); or for

initial scout work, used to determine the best locations for sectioning (Ketcham & Carlson, 2001).

Biomedical micro-CTs are the ideal machines to utilize in geomaterial analysis; this is because they are: 1) more common than high-energy machines; 2) are installed at various university research centers; 3) exhibit high spatial resolution on small specimens; and 4) allow the specimen to remain stationary (in comparison to industrial scanners that typically rotate the specimen, potentially disrupting samples). Unfortunately, many scanners (particularly widely available biomedical scanners) may not have an adequate dynamic range to study dense objects and often are only available with a lower peak voltage (90 – 120 kVp) when compared with industrial scanners (>200 kVp).

Artifacts due to dense materials can lead to incorrect reconstructed signal levels in the interior of specimens, confounding analysis, and can also lead to streak artifacts that obscure details both on the interior and exterior of the specimens. The major sources of these errors include: beam hardening, an artifact due to the preferential removal of low-energy photons in a polyenergetic spectrum; photon scatter; and under-ranging, inadequate dynamic range manifested as inadequate recording of very dark signals.

Proposed herein is a simple correction for X-ray beam hardening and scatter that can be readily applied to available biomedical scanners. The correction takes the form of a semi-empirical calibration algorithm that can be applied to X-ray transmission data. This method of post-processing can be applied retrospectively to existing data, offering the ability to re-evaluate previously scanned specimens (provided that original transmission data have been preserved). The calibration data are acquired using materials of known composition and thickness at specific acquisition protocols. Numerical fits to the empirical calibration data are generated to produce a correction function that is able to linearize the log transmission CT data, reducing or removing artifacts (such as cupping and streaks). The proposed correction algorithm is described, implemented, and tested on two current biomedical CT scanners. Two numerical fits are explored for two separate calibration materials and evaluated for their ability to reduce or remove the aforementioned artifacts.

## 2.2 Methods

### 2.2.1 Theoretical basis of the correction algorithm

Beer's law states:

$$I = I_o e^{-\mu x}$$

where  $I$  is the measured intensity at the detector,  $I_o$  is the incident intensity from the source,  $\mu$  is the linear attenuation of the materials in the photon path, and  $x$  is the perpendicular distance from source to detector through the materials. This expression describes the expected response for each material inside a CT scanner. Dividing  $I$  by  $I_o$  and taking the natural logarithm, we produce:

$$\ln(I_o/I) = \mu x$$

We define  $\ln(I_o/I)$  as  $T$  (transmission) and produce the linear function:

$$T = \mu x \quad \text{[Equation 1]}$$

Therefore transmission, the natural logarithm of incident intensity over measured intensity, should be linearly proportional to  $\mu$ , the linear attenuation of a given material. Any deviation from linearity in plot of transmission over thickness will give rise to errors and artifacts. The two main processes responsible for this deviation are beam hardening and scatter. *Both* processes lead to the detection of excess photons, which is erroneously reported as increased transmission. Hence, we are left with an underestimation of the material's attenuation co-efficient ( $\mu$ ), resulting in cupping. *Figure 2.1* shows the effect and the deviation from the expected linear relationship in transmission values.

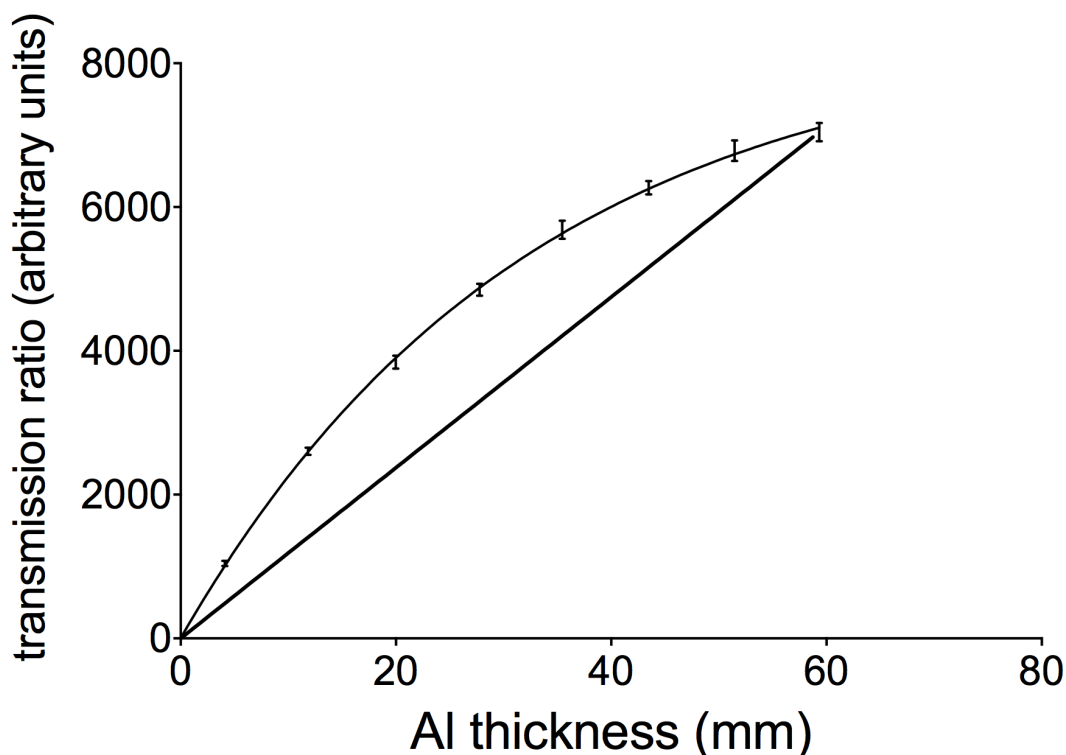


**Figure 2.1 - Plot of transmission vs. thickness for aluminum calibrator.** CT scans of the aluminium calibrator were completed on the speCZT at 90 kVp and 40 mA. This plot shows the non-linearity of thickness to transmission ratio of photons. The straight line represents the expected linear response.

The correction function is based on a curve fit to empirical data. A calibration object of one material and various known thicknesses, covering the range of application, was developed. Following this, transmission data at each thickness was collected for each acquisition protocol for which correction is to be performed; these data were then fit to an appropriate functional form. The fitted function can then be used to create a look-up table, which remaps the observed transmission data to linearized corrected values on a pixel-by-pixel basis, for each projection view. Previous authors have used point-to-point linear (Chen et al., 2001) and polynomial (Herman, 1979) fits. Herman's original beam hardening corrections also showed that polynomial fits gain little improvement with degrees higher than two (Herman, 1979). Based on the departure from linear as observed in *Figure 2.1*, we may also consider a functional form that increases monotonically to a



plateau value, such as an inverted one-phase (inverse) decay described by the following equation:

$$T=(T_o - P)e^{(-K*x)} + P \quad \text{[Equation 2]}$$

where  $T_o$  is the  $T$  value when  $x$  is zero.  $P$  is the  $T$  value at infinite time,  $K$  is the rate constant;  $x$  is the perpendicular distance from source to detector. This function provides the advantage that it can be extrapolated beyond the global maximum of a second-degree polynomial. In this work, both inverse decay and second-degree polynomial fits will be implemented and compared.

### 2.2.2 Biomedical micro-CT scanners

Two laboratory micro-CT scanners were used in this study to validate the versatility of the methods. Both a GE Locus Ultra (Ultra) and GE eXplore speCZT (speCZT) were utilized. Scans on the Ultra were completed at an X-ray tube voltage of 120 kVp and current of 20 mA in a 24 cm bore, with reconstruction over a 15 cm field-of-view (FOV). For each scan, 1000 views were obtained in  $0.365^\circ$  increments at an exposure time of 16 ms per frame. These scan parameters resulted in an acquisition duration of approximately 5 minutes and are reconstructed at a  $150 \mu\text{m}$  isotropic voxel spacing. Scans performed on the speCZT were completed at an X-ray tube voltage of 90 kVp and current of 40 mA using the large focus of the X-ray tube in a 8.9 cm bore, with reconstruction over a 70 mm FOV. For each scan, 900 views were obtained in  $0.4^\circ$  increments at an exposure time of 16 ms per frame. These scan parameters resulted in an acquisition duration of approximately 5 minutes and are reconstructed at  $50 \mu\text{m}$  isotropic voxel spacing. Both scanners utilize rotating source-detector geometry, allowing the sample to remain stationary during the scanning process, thus minimizing the disruption of sensitive samples, a feature particularly important for pore and flow analysis of soils. These machines rely on cone-beam geometry where the reconstruction occurs on a set of 2D projection images. Reconstruction of the post-processed transmission data occurs using the manufacturer supplied reconstruction algorithms and binned  $2 \times 2 \times 2$ , with corrected projections being replaced before reconstruction.

In these scanners, as is typical, the raw X-ray images are corrected to produce transmission images following *equation 1*; pixel-to-pixel variations and known geometric distortions are corrected simultaneously. To create a calibration curve that describes the observed transmission values for fitting, only a single projection of each calibration thickness is necessary. A single-view protocol is used, ensuring the source-detector system is perpendicular to the known thickness of the calibration phantom. This allows for measurement of the transmission data at each thickness. ImageJ software (National Institutes of Health, Bethesda, MD) was utilized for interpretation of the data, wherein an ROI is chosen that accurately represents the observed transmission through the calibration phantom.

Two phantom materials were chosen: water-like PMMA (Poly[methylmethacrylate], or Lucite), due to its current use in tissue-level beam hardening correction (Chen et al., 2001); and aluminum, to mimic dense objects like bone, silicate minerals, and other geomaterials with similar electron densities. The observed data were fitted to each of the proposed correction functions and a custom-written software routine corrected each transmission projection view in a pixel-by-pixel fashion, linearizing the transmission values from the previously observed values. Care must be taken to avoid wrap-around or over ranging of the transmission images. If values are stored in a fixed-width integer (e.g. signed short integer) it may be necessary to use extended dynamic range acquisition scaling, if provided by the manufacturer.

### 2.2.3 Calibration phantom

The calibration phantoms are designed and manufactured in house. They are each a single object comprised of eight coaxial cylinders with diameters ranging from 4.5 mm to 60 mm; two opposing sides were flattened in a 20° arc to provide larger measurement locations. Two calibrators were employed, one of 6.35 mm thick aluminum (6061-T6) and one of 4.7625 mm thick PMMA. The calibrators are designed in an alternating step configuration to mimic the irregular nature of specimens, in an effort to simulate typical scatter profiles, as seen in *Figure 2.2*. A single projection can be collected at the intended scanner and acquisition protocol (*Figure 2.3*) and the calibration phantom's eight thicknesses provide measurements for the range of calibration. Alternatively, many

materials can be used to create various calibration phantoms for intended needs; for example, concrete forms of several thicknesses could be used to calibrate for scans of concrete cylinders. These calibration scans must be performed at the same acquisition parameters that the corrected object is to be scanned, particularly with respect to kVp.

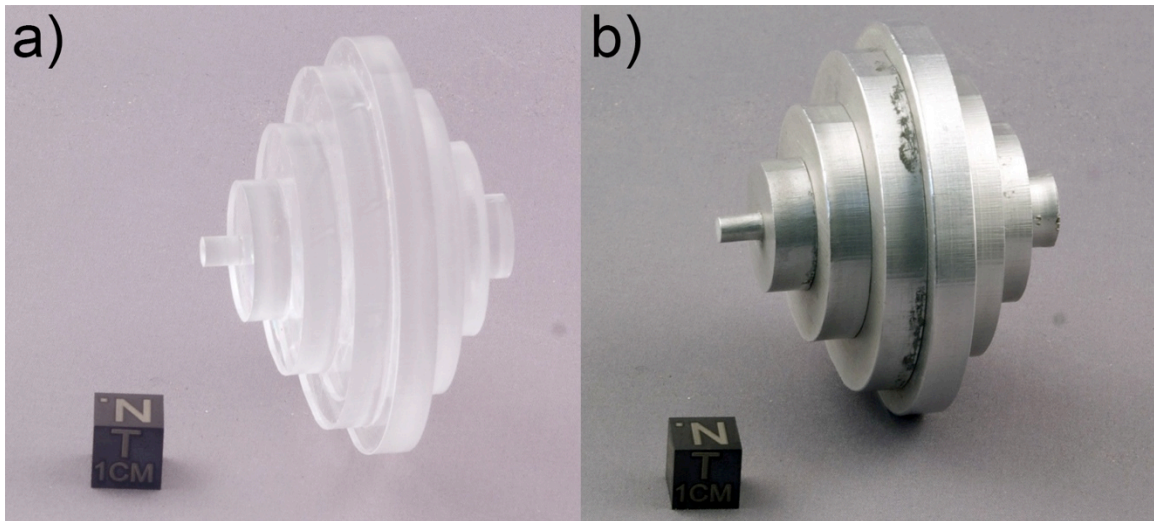


**Figure 2.2 - Calibration phantoms for beam hardening correction in CT.** Phantoms were fabricated from a) PMMA and b) Aluminum by gluing disks of various diameters to each other in an alternating fashion. Scale cube (1 cm) for size reference.

#### 2.2.4 Data analysis

The fitted functions of the transmission data were completed using non-linear Levenberg Marquard fitting in Prism (GraphPad Software, Inc., La Jolla, CA). A second-degree polynomial was chosen to match the current methods in the literature (Herman, 1979; So et al., 2009) as well as an inverse decay function (Eq. 2), chosen due to its increasing nature that plateaus at a maximum value. Each function was constrained to pass through the origin to mimic real world expectations. Both these fits were performed on aluminum and PMMA data from both the Ultra and speCZT machines.

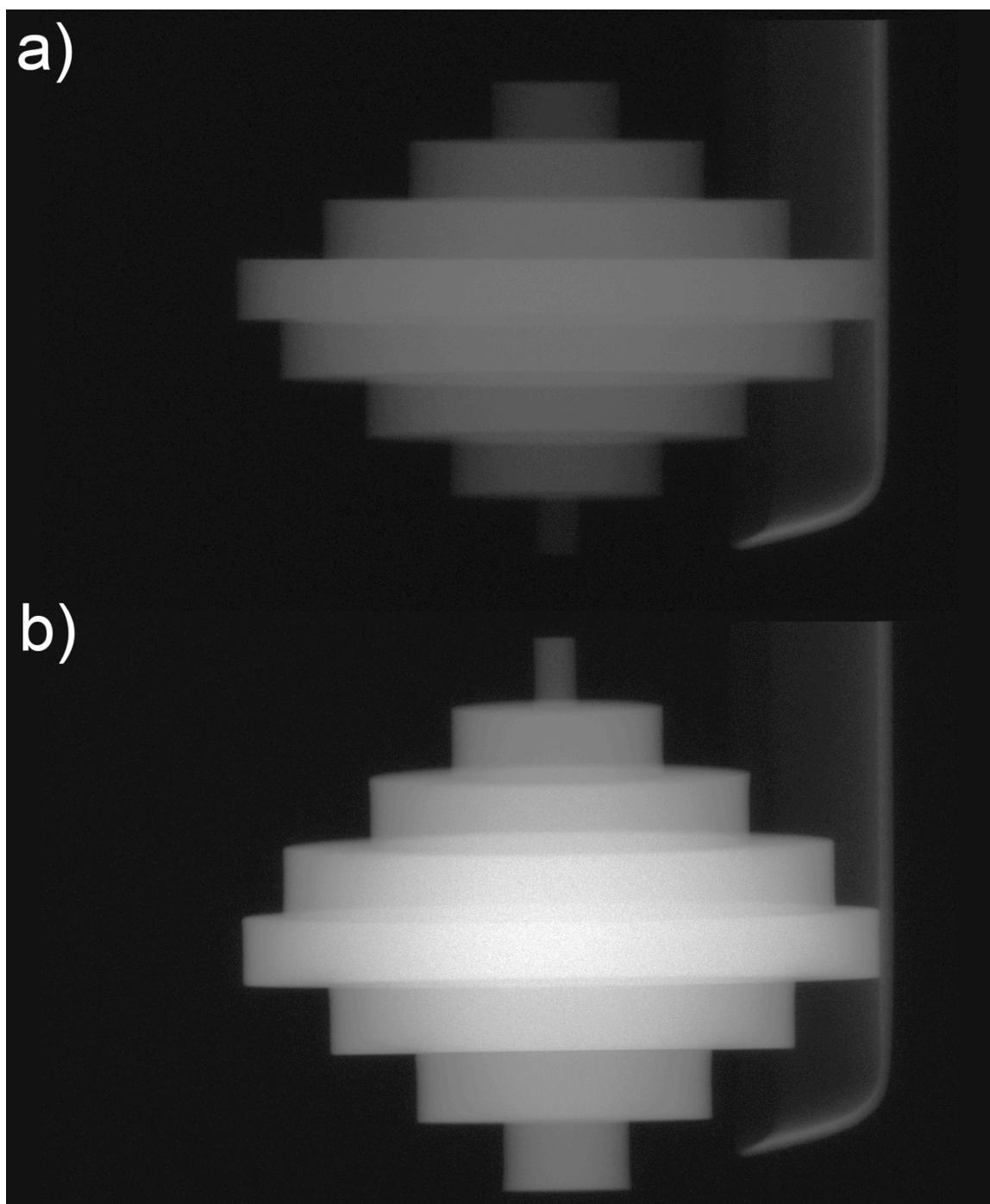


**Figure 2.3 - Transmission images of CT calibration phantoms.** Scans were performed on both a) PMMA and b) aluminum calibration phantoms using the speCZT scanner at 90 kVp and 40 mA. Images from the Ultra scanner (which appear the same) were used for corresponding calibration.

Scans were performed on both PMMA and aluminum rods of various diameters, and then reconstructed natively (no correction or uncorrected) and with beam-hardening corrected projections to examine the range over in which the correction is possible. Rods of a single material were chosen as phantoms to evaluate the correction as the single material provides an easy way to check the uniformity of the correction and the uniform cylindrical shape is not only a good model for CT uniformity but also approximates the intended sample shapes. PMMA was corrected by using all four correction algorithms (two calibration phantoms with two mathematical fitting methods each), examining the possibility to correct materials of lower attenuation using calibration fits obtained with more attenuating materials. Aluminum rods of various diameters were scanned and reconstructed uncorrected and by using both mathematical aluminum corrections to evaluate the separate fitting methods. This also ensures that the corrections work as intended. These scans were performed on each machine at the same acquisition parameters as the calibration phantoms. Using ImageJ, 4x4 px regions of interest (ROIs) were taken at the center of the rods, the edge of the rods, and in the air surrounding the rods, demonstrated in *Figure 2.4*. Percent cupping (described below), line profiles and images through five slices of each sample were then evaluated. The percent cupping on each profile is described by

$$\%Cupping = 1 - ((C-A)/(E-A)) \quad [Equation 3]$$

where E, C and A are the average voxel value in the edge, center and air, respectively. This produces a result that measures the amount of cupping artifact that occurs in the center of the object, compared to the edge (where the artifact is less predominant due to shorter path lengths). Each result is compared against the uncorrected reconstruction.

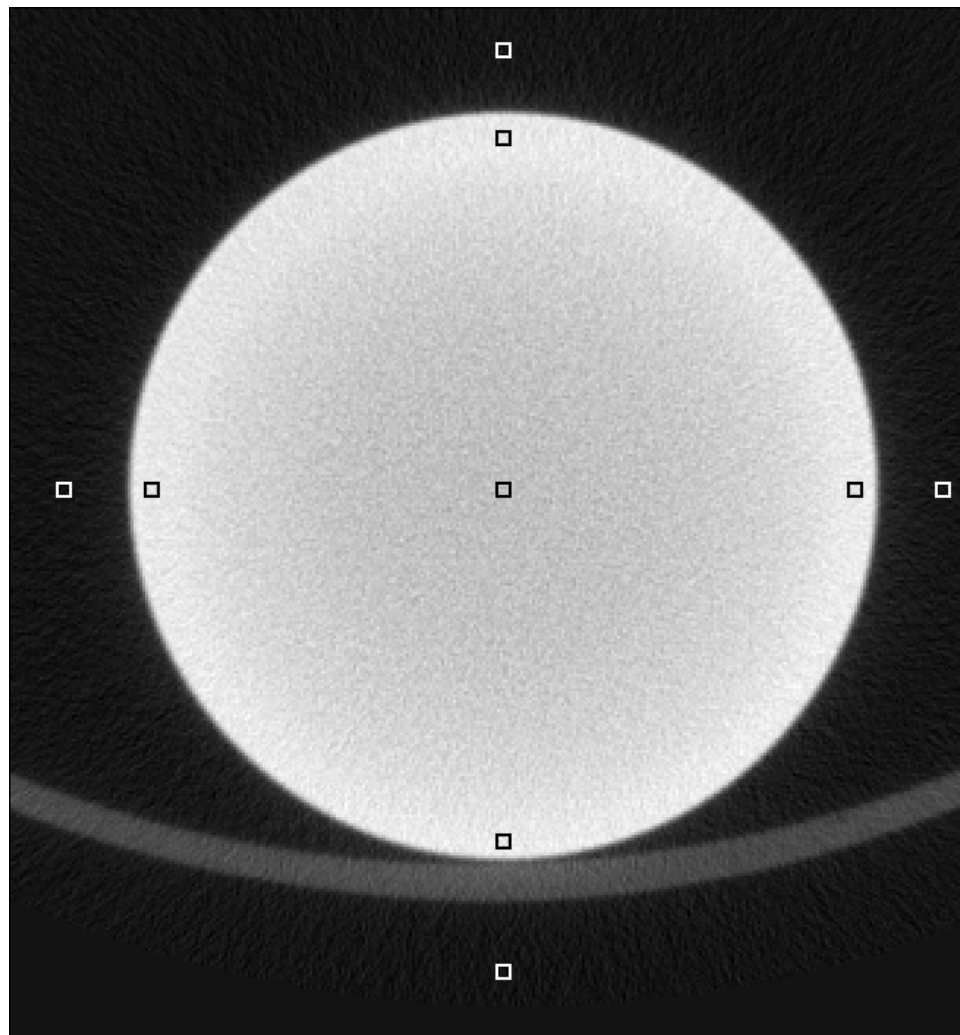


**Figure 2.4 - Locations of the ROI measurements used for percent cupping analysis.** Nine ROI measurements, here shown on 63.5 mm rod, from selected CT scan planes were taken on each testing rod. Four measurements were taken in the edges of the object, four in the surrounding air and one in the center of the object.

#### 2.2.4.1 Calibration data

Single transmission projections were analyzed using 4x4 px ROIs within the calibrator's flat sections. The areas were measured and averaged using ImageJ as shown in *Figure 2.3*, and following this, Prism was used to fit and analyze the data. Calibration curves for each the speCZT and Ultra scanners were fit to the calibration data for each material, resulting in 4 calibration fits per scanner. A second-degree polynomial fit to both PMMA and aluminum and inverse decay fit to PMMA and aluminum were examined.

## 2.2.4.2 Reconstruction analysis

Using ImageJ on corrected and uncorrected reconstructions of the aforementioned rods, line profiles were constructed and percent cupping was calculated, following *equation 3*. Line profiles were measured along the diameter within a slice of each rod. Additionally on each of these slices, nine 4x4 voxel ROIs were measured; four within the edges of the rod, four within the air surrounding the rod and an additional ROI placed within the center of the rod as illustrated in *Figure 2.4*. The measurements of the three regions were averaged before percent cupping was calculated. Averages and standard deviations of percent cupping between each slice were calculated within Prism.

## 2.3 Results

### 2.3.1 Calibration data

All fits proved to be highly accurate ( $R^2 > 0.99$ ). Both scanners yielded similar fitting results, but note that the individual values vary as both scanners store transmission values in different data types and scale the data differently (using arbitrary scaling constants), as shown in *Figure 2.5* and *Figure 2.6*, and summarized in *Table 2.1*.

**Table 2.1 - Formulas and coefficients of determination for each fitting parameters.**

		Ultra	speCZT
Lucite	Polynomial	$y = -2.431 \times 10^{-5}x^2 + 0.02380x$ $R^2 = 0.9999$	$y = -0.09079x^2 + 51.49x$ $R^2 = 0.9999$
	One-phase decay	$y = -10.97e^{-0.002173x} + 10.97$ $R^2 = 0.9999$	$y = -13235e^{-0.003904x} + 13235$ $R^2 = 0.9999$
Aluminum	Polynomial	$y = -0.0005034x^2 + 0.08642x$ $R^2 = 0.9999$	$y = -1.858x^2 + 227.6x$ $R^2 = 0.9977$
	One-phase decay	$y = -5.281e^{-0.01723x} + 5.281$ $R^2 = 0.9996$	$y = -8445e^{-0.03102x} + 8445$ $R^2 = 0.9995$

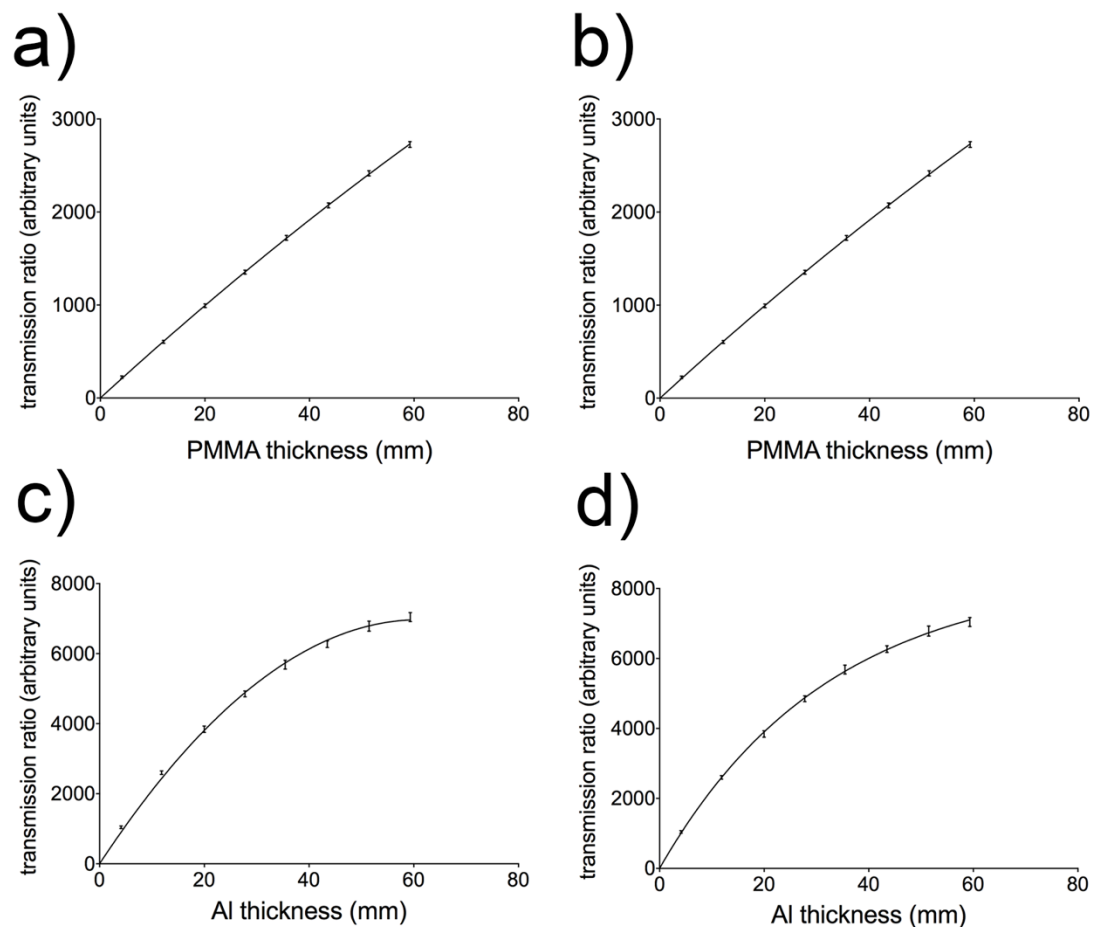


**Figure 2.5 - Plots of transmission ratio vs. thickness of calibration phantoms in speCZT scanner.** CT scan data of both calibration phantoms acquired from speCZT (90 kVp, 40 mA) were used to construct transmission ratio vs. thickness plots of the PMMA calibrator data with a) polynomial fit, b) one-phase inverse decay fit, and aluminum calibrator data with c) polynomial fit and d) one-phase inverse decay fit.



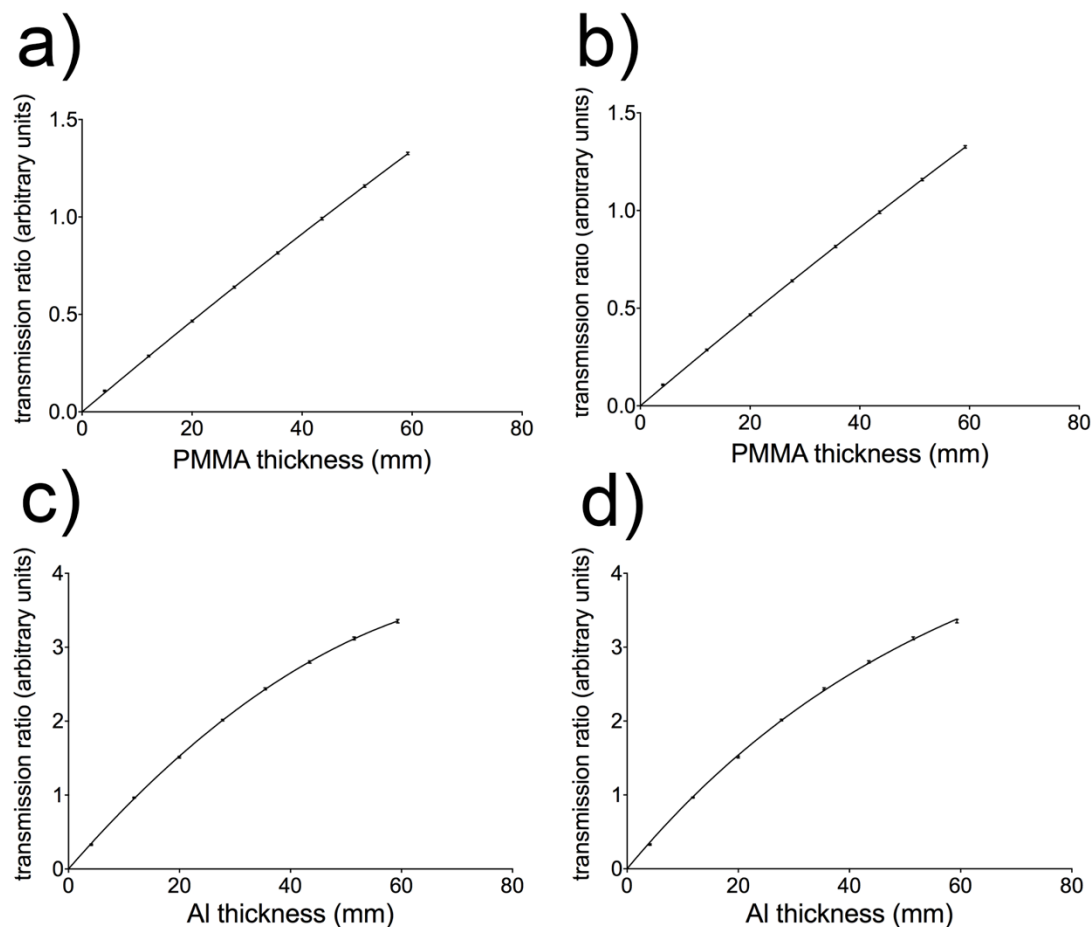


**Figure 2.6 - Plots of transmission ratio vs. thickness of calibration phantoms in Ultra scanner.** CT scan data of both calibration phantoms acquired from Ultra (120 kVp, 20 mA) were used to construct transmission ratio vs. thickness plots of the PMMA calibrator data with a) polynomial fit, b) one-phase inverse decay fit, and aluminum calibrator data with c) polynomial fit and d) one-phase inverse decay fit.

### 2.3.2 Reconstruction analysis

The data for PMMA phantom correction and aluminum phantom correction are summarized for each in *Table 2.2* and *Table 2.3*, respectively. The correction methods are labeled as the following: PMMA PN and PMMA ID refer to the polynomial and inverse decay fits to the PMMA calibration phantom, respectively. Al PN and Al ID refer to the polynomial and inverse decay fits to the aluminum calibration phantom, respectively.

**Table 2.2 - Average and standard deviation of percent cupping in PMMA data described by equation 3, for CT scanners a) speCZT and b) Ultra.**

a)	mm	Original		PMMA PN		PMMA ID		Al PN		Al ID	
		Percent Cupping	Std Dev	Percent Cupping	Std Dev	Percent Cupping	Std Dev	Percent Cupping	Std Dev	Percent Cupping	Std Dev
	15.88	-1.18	1.00	-2.57	1.01	-2.66	1.00	-2.53	0.98	-3.51	1.03
	22.23	-0.27	1.94	-2.66	2.07	-2.78	2.07	-2.57	2.06	-4.18	2.11
	31.75	2.69	2.49	-1.12	2.74	-1.19	2.68	-0.98	2.67	-3.50	2.84
	38.10	3.33	1.54	-1.31	1.58	-1.39	1.56	-1.08	1.73	-4.28	1.86
	63.50	12.88	1.70	4.91	2.07	5.02	2.07	5.85	2.10	0.61	2.31

b)	mm	Original		PMMA PN		PMMA ID		Al PN		Al ID	
		Percent Cupping	Std Dev	Percent Cupping	Std Dev	Percent Cupping	Std Dev	Percent Cupping	Std Dev	Percent Cupping	Std Dev
	15.88	-1.81	0.30	-2.57	0.31	-2.60	0.31	-3.04	0.32	-3.51	0.33
	22.23	-1.53	0.81	-2.78	0.82	-2.82	0.82	-3.58	0.83	-4.34	0.85
	31.75	-1.13	0.68	-3.22	0.71	-3.27	0.71	-4.63	0.73	-5.89	0.75
	38.10	0.68	0.72	-2.29	0.61	-2.33	0.61	-4.27	0.67	-6.00	0.71
	63.50	4.18	1.26	-0.86	1.45	-0.81	1.45	-4.76	1.63	-7.68	1.74

**Table 2.3 - Average and standard deviation of percent cupping in aluminum data described by equation 3, for CT scanners a) speCZT and b) Ultra.**

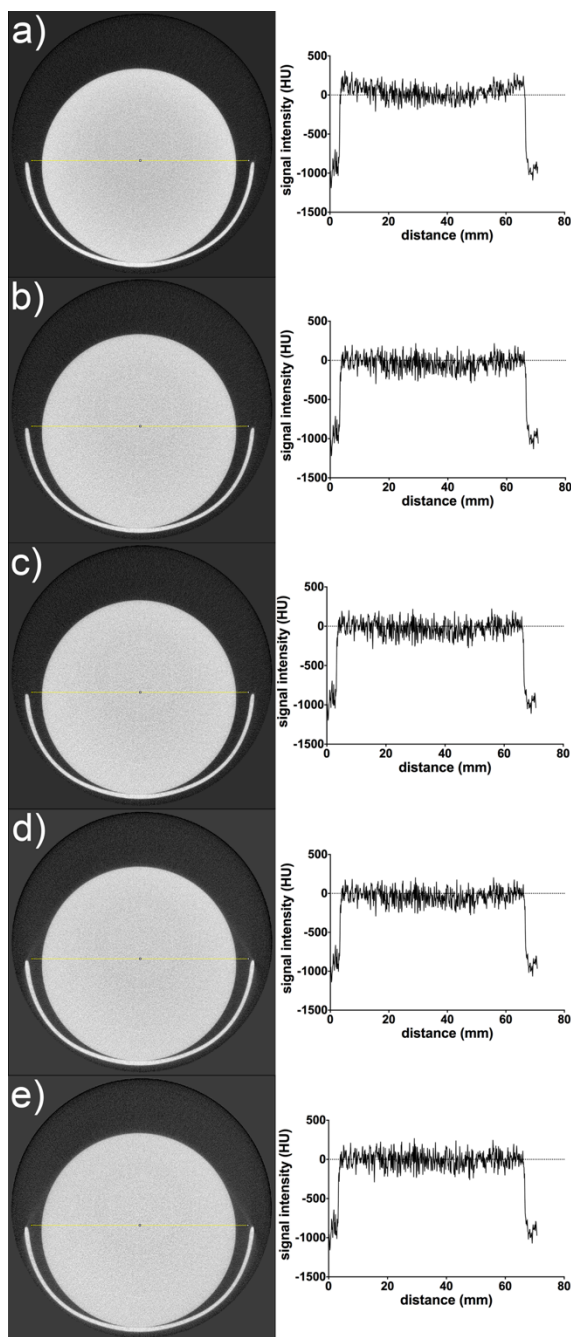
a)	mm	Original		Al PN		Al ID	
		% Cupping	SD	% Cupping	SD	% Cupping	SD
	12.70	7.07	0.76	1.06	0.95	-2.74	1.05
	18.38	13.75	0.79	3.49	1.06	-2.71	1.22
	25.40	20.48	1.44	4.07	2.17	-5.59	2.58
	38.10	27.97	1.57	-1.5032	3.83	-14.15	4.59
	50.80	33.79	1.76	-45.85	19.44	-34.52	8.10

b)	mm	Original		Al PN		Al ID	
		% Cupping	SD	% Cupping	SD	% Cupping	SD
	12.70	1.90	0.54	-2.09	0.56	-3.42	0.58
	18.38	4.75	1.17	-1.54	1.48	-3.38	1.57
	25.40	8.95	0.76	-0.65	0.95	-3.05	0.95
	38.10	14.86	1.56	-3.16	3.06	-5.59	3.06
	50.80	21.56	1.85	-8.52	5.22	-7.40	4.25

### 2.3.2.1 PMMA samples

Cupping artifacts within PMMA increase with rod diameter in the uncorrected samples, this is observed within both scanners. The differences between acquisition protocols cause variations in the amount of cupping seen in the individual samples. Small diameter samples have little cupping and PMMA calibrated corrections improve the cupping ( $P < 0.0001$ ) or do little to modify it; however, the PMMA PN correction results in smaller cupping values across the range of samples compared to PMMA ID. On the Ultra, aluminum calibrated corrections perform worse than the PMMA calibrated corrections, causing values in the center to be higher than the edges of the sample (herein referred to as overcorrection). However, on the speCZT the aluminum calibrated corrections outperform those calibrated with PMMA. The Al PN correction performed better than the Al ID correction in all the samples examined, and in the speCZT protocol it performed similarly to the PMMA ID correction keeping the central values within 5% of the edges. These data are summarized in *Table 2.2* and on the line profiles in *Figure 2.7* and *Figure 2.8*.



**Figure 2.7 - Correction of 63.5 mm PMMA rod scanned on speCZT with image and line profile.** CT scan planes and corresponding line profiles of a 63.5 mm PMMA rod scanned on the speCZT (90 kVp, 40 mA) following a) no correction, and correction methods as obtained from the PMMA calibrator using b) polynomial fit, c) one-phase inverse decay fit, and the aluminum calibrator using d) polynomial fit and e) one-phase inverse decay fit.

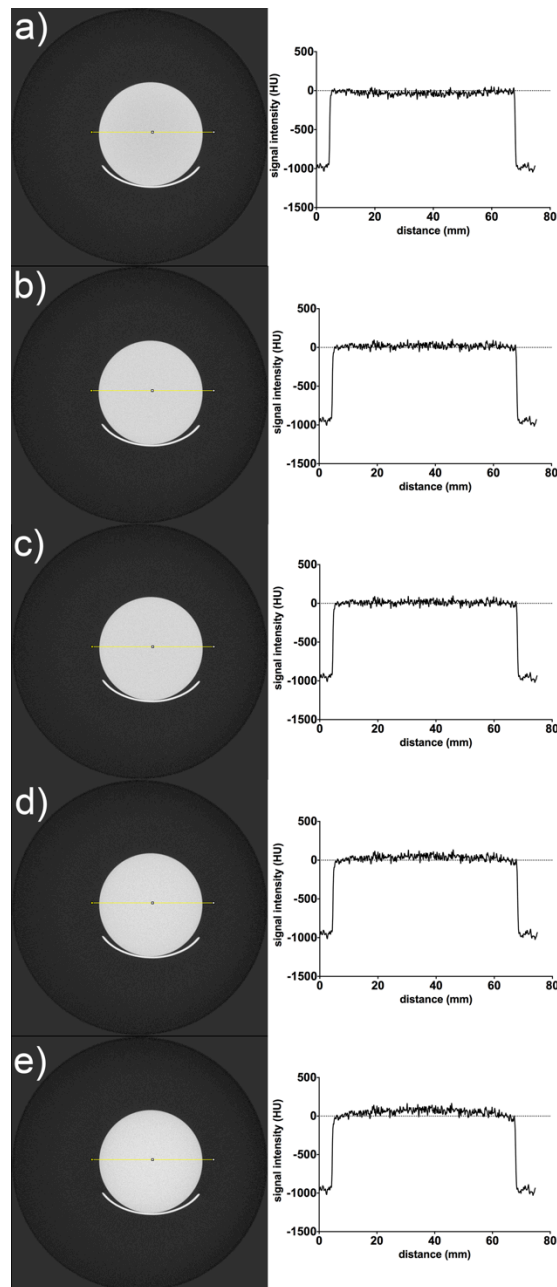


**Figure 2.8 - Correction of 63.5 mm PMMA rod scanned on Ultra with image and line profile.** CT scan planes and corresponding line profiles of a 63.5 mm PMMA rod scanned on the Ultra (120 kVp, 20 mA) following a) no correction, and correction methods as obtained from the PMMA calibrator using b) polynomial fit, c) one-phase inverse decay fit, and the aluminum calibrator using d) polynomial fit and e) one-phase inverse decay fit.

### 2.3.2.2 Aluminum samples

As with PMMA, cupping artifacts within the aluminum rods increase with rod diameter. After correction, both polynomial and inverse decay corrections are able to improve cupping artifacts ( $P < 0.0001$ ). Al PN outperformed inverse decay across the range of samples, resulting in smaller amounts of cupping, however both show improvement over uncorrected samples. Within the Ultra protocol both corrections had a tendency to overcorrect the samples, however the absolute cupping was still reduced; this tendency also occurred within PMMA ID corrections of the spcCZT samples. These data are summarized in *Table 2.3* and on the line profiles in *Figure 2.9* and *Figure 2.10*. On the speCZT the 50.8 mm sample caused extreme cupping, exceeding 30%. When correction was attempted on this sample very high noise values and over correction occurred as detailed in the discussion.

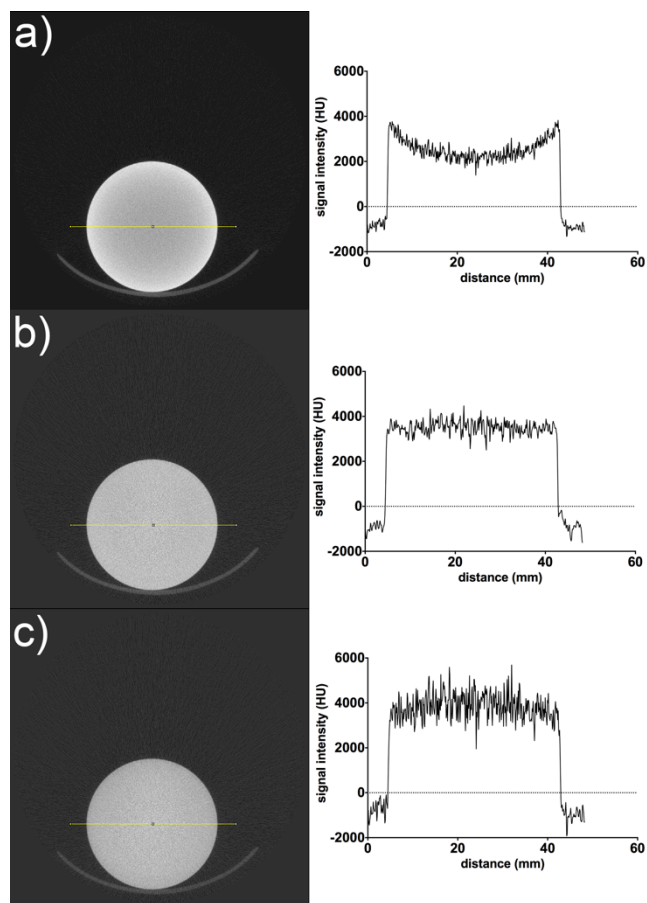


**Figure 2.9 - Correction of 38.1 mm aluminum rod scanned on speCZT with image and line profile.** CT scan planes and corresponding line profiles of a 38.1 mm aluminum rod scanned on the speCZT (90 kVp, 40 mA) following a) no correction, and correction methods as obtained from the aluminum calibrator using b) polynomial fit and c) one-phase inverse decay fit.

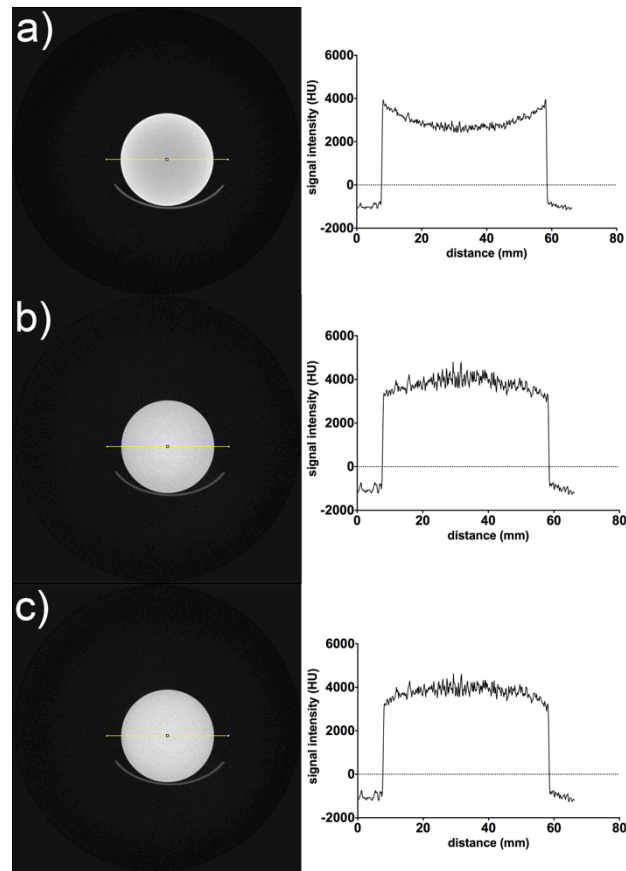


**Figure 2.10 - Correction of 50.8 mm aluminum rod scanned on Ultra with image and line profile.** CT scan planes and corresponding line profiles of a 50.8 mm aluminum rod scanned on the Ultra (120 kVp, 20 mA) following a) no correction, and correction methods as obtained from the aluminum calibrator using b) polynomial fit and c) one-phase inverse decay fit.

## 2.4 Discussion

The reduction of cupping artifacts within samples is possible with the introduction of a linearization process to the projection data, provided that adequate calibration data have been obtained at the same scanning protocol. The prescribed alternating step calibration phantom has proven itself to be a quick and efficient way to collect and measure the calibration data. Due to variability within scanning systems it is advisable to not assume that there is a consistent correction method compatible with all systems or acquisition protocols. However, with little effort it is possible to determine the correct correction method for a predetermined protocol.



### 2.4.1 GE eXplore speCZT

On our speCZT system (90 kV, 40 mA), Al PN performed better than Al ID in three of the four different sized aluminum rods. It was effective at correcting rods up to 38.1 mm in diameter, where it was able to reduce cupping from 28% to -1.5%. Additionally, this correction method was able to outperform Al ID as well as both the PMMA PN and ID corrections in PMMA rods of up to 38.1 mm in diameter; calibrations that were specifically designed for that material. In the 63.5 mm diameter rod it failed to produce optimal results. However, it was able to reduce cupping from 12.9% to 5.85%, compared to the best reduction of 4.91% by PMMA PN. Given these specific set of circumstances (scanner, protocol and phantom), we found Al PN to be the most effective beam hardening correction algorithm.

The 50.8 mm rod resulted in a very large total attenuation, causing inadequate photon capture by the scanner. This decreased photon capture causes the noise of the reconstruction to increase significantly after correction due to cupping, causing large coefficient of variations in the center of the object. This causes the cupping measurement to become unreliable in those reconstructions and noise levels to reach unacceptable levels. Although correction is possible in larger objects at higher energy scanning, as seen in the same sample scanned on the Ultra, the scan parameters used on the speCZT (90 kV, 40 mA) did not provide enough flux; these results are illustrated as line profiles in *Figure 2.11*. This upper limit to correction, where the photon starvation is too large to overcome with re-linearization of the projections, is a limitation of the available flux from the scanner on a specified total attenuation.

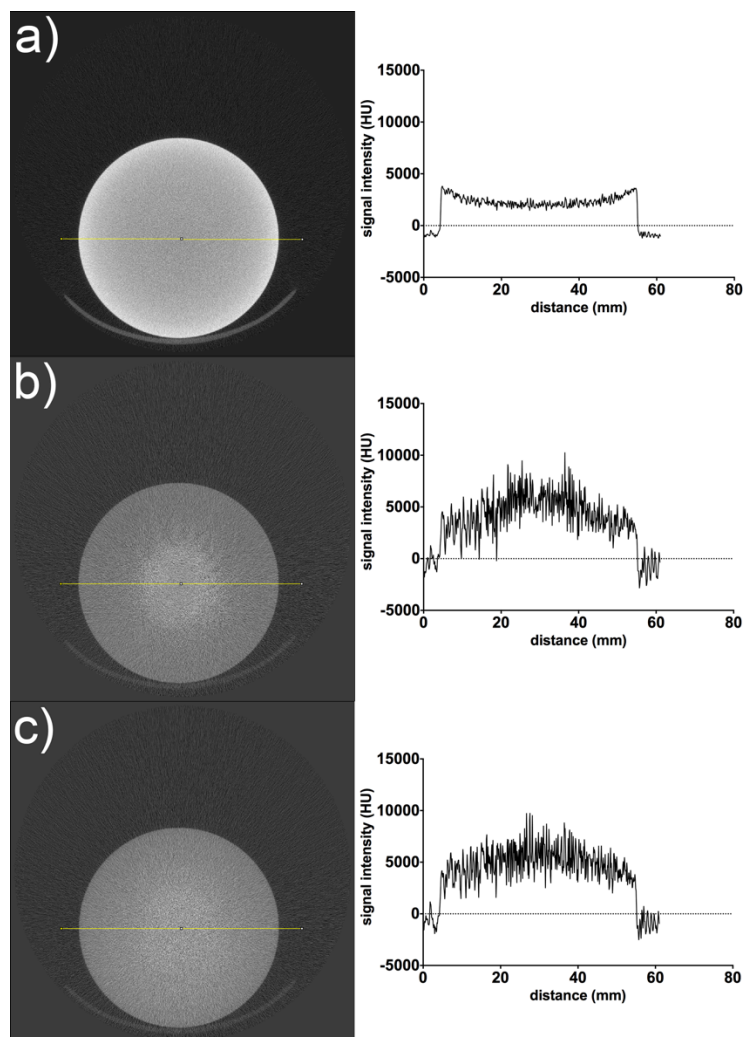


**Figure 2.11 - Correction of 50.8 mm aluminum rod scanned on speCZT with image and line profile.** CT scan planes and corresponding line profiles of a 50.8 mm aluminum rod scanned on the speCZT (90 kVp, 40 mA) following a) no correction, and correction methods as obtained from the aluminum calibrator using b) polynomial fit and c) one-phase inverse decay fit. In this scan, the parameters used on the speCZT did not provide enough flux.

## 2.4.2 GE Locus Ultra

On our Ultra system (120 kV, 20 mA) Al PN performed better than Al ID in four of the five different sized aluminum rods. In the 50.8 mm diameter rod it failed to produce optimal results, reducing cupping from 21.6% to -8.5% compared to the best reduction of -7.4% by Al ID. Additionally, this correction method was able to outperform Al ID in all

of our PMMA rods. However, in contrast to the speCZT system, Al PN was not able to outperform either PMMA PN or ID. In these conditions, there is little cupping without correction with the 63.5 mm rod, resulting in 4.2% cupping prior to correction. Al PN performed adequately in this situation, especially when considering situations where both high- and low-density regions are within the scan object. Given this specific set of circumstances (scanner, protocol, phantom), we found Al PN to be the most effective beam-hardening correction algorithm.

### 2.4.3 Summary, limitations, and future work

Semi-empirical corrections for beam hardening have been described and adopted in the past, originally described in 1976 (Brooks & Di Chiro, 1976). This method of linearizing the transmission data based on *a priori* knowledge can reduce cupping artifacts, which include artificially low attenuation coefficient in the center of reconstructed objects, and improve interface contrast. This method was further explored in 1979, showing that second degree polynomial fitting of the beam hardened data can provide excellent correction to beam hardening within human tissue (Herman, 1979), and that higher degree polynomials provide little improvement over a quadratic fit. Beam hardening can be reduced at the cost of photon flux by the use of filtration, and has been shown to reduce cupping in water phantoms (Meganck et al., 2009). A post-reconstruction method using re-projections of CT objects and corrections using curves based on aluminum has been shown to reduce beam hardening in aluminum up to 14% (Chen et al., 2001). These methods employ an intermediate stage correction, performed on the original or re-projection of CT data, and can correct cupping artifacts and extend the dynamic range and accuracy of biomedical scanners when applied to geomaterials. The only difficulty in applying these corrections is that some knowledge of the CT reconstruction process is required, as well as accurate calibration data measured from the scanner to apply a semi-empirical correction. Methods involving dual energy CT with fast switching between energies have been proposed and shown to work (Kalender et al., 1986), even working during myocardial perfusion (Yamada et al., 2012); these methods, however, require specific scanners and methods to produce these results.

Although we have found aluminum calibrated, polynomial fitted, beam hardening correction to be the most effective algorithm overall, in order to obtain optimal results specific to one's scanner and protocol, it may be required initially to reconstruct and analyze calibration data. Results may vary depending on the system and acquisition protocol. Specific situations may also have different requirements and measures of effectiveness. In situations where materials within a close range of X-ray attenuation are being examined, measures of modification for materials with lower attenuation would be unnecessary.

This method is highly modifiable for specific situations and it is advisable to change the methodology for situations for which there could be a benefit. It is always advisable to scale the calibration phantoms to a size comparable to objects that will routinely be scanned. Making calibration phantoms out of different materials has the advantage of providing calibration data specific to scan conditions. With proper equipment it would be possible to mimic our calibration phantom out of various geomaterials, both homogeneous (e.g. clay) and heterogeneous (e.g. granite), which can provide beneficial results for further examination of those materials. The design of our phantom provides the advantage that only one projection image is required to obtain all of the necessary calibration data.

It is important to remember the limitations of individual protocols and scanners; low voltages and currents limit the ability to correct scans adequately. As seen in the large samples of aluminum, it is difficult to properly correct these samples when scanned at lower energies, and corrections yield undesirable results. Therefore it is always advisable to scan materials, and corresponding calibrators, in situations that provide ample photon collection through the highest attenuating paths while ensuring there is no over ranging occurring in paths of lower attenuation.

Within this study, only two function forms were examined. It would be beneficial to examine other forms as they could potentially provide more accurate fits or better reconstruction results. Additionally, only two scanners with a single protocol on each were examined. While this methodology will likely scale to other scanners easily, further

work could serve to ensure this. Future work to be pursued could also include repeating this study at various protocols on the same scanner in order to provide correction across the range of protocols regularly used. It would also be beneficial to run two scanners at the same energies to see if similar results are obtained. A multi-variable study could also be implemented to examine the change in function forms over various protocols; patterns may emerge to allow for prediction of functional forms without calibration scanning.

Testing of calibration on various real world geomaterial samples is a logical next step. As continued in Chapter 3, this method can readily be applied to various geomaterials. As shown in *Figure 2.12*, this method has been applied to the meteorite Gao Guenie (H5 chondrite). It can easily be seen that major parts of the uncorrected volume are not incorporated above the threshold whereas post-correction more of the volume is above the threshold. This is the basis for threshold volume calculations and accurate thresholding is necessary for accurate volume analysis.

There are two distinguishable phases in the sample, a high radiodense metallic phase, consisting of kamacite and taenite, is surrounded by the bulk material. Veins of sulphides are said to be found in some samples of Gao-Guenie (Bourot-Denise et al., 1998) and any within this sample would appear similar to the metallic content. Performing volumetric measurements on these regions resulted a total volume of 2535.2 mm<sup>3</sup> for the uncorrected sample and 2549.9 mm<sup>3</sup> for the corrected volume. These don't differ much as the correction adds little ability to segment the volume from the surrounding air. The internal metallic content was measured as 292.9 mm<sup>3</sup> and 456.9 mm<sup>3</sup> for the uncorrected and corrected volumes respectively. This results in a metallic content estimation of 12% v/v for the uncorrected volume and 18% v/v for the corrected volume. These data is summarized in *Table 2.4*

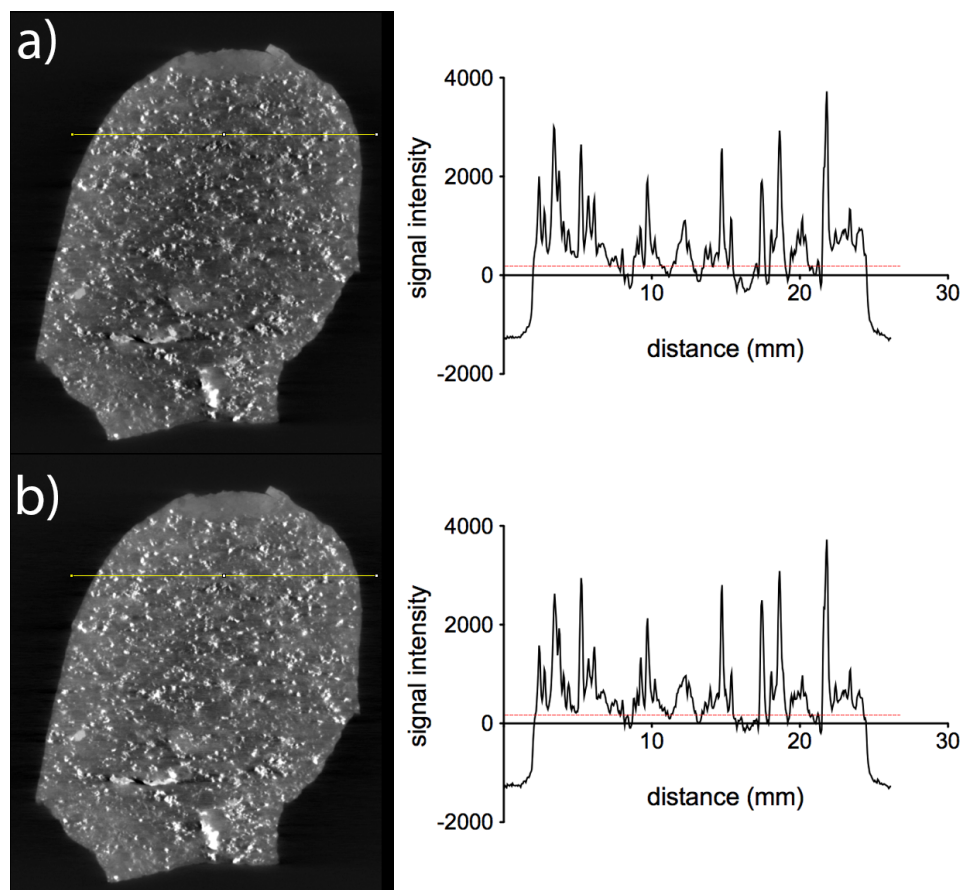


**Figure 2.12 – Pre and Post-Correction of Gao Guenie with line profile.** Gao Guenie and associated line profile a) uncorrected and b) corrected with aluminium one-phase decay correction. Bright spots indicate material of high radiodensity, mainly kamacite and taenite, surrounded by the silicate bulk material.

**Table 2.4 - Volumetric Analysis for Corrected and Uncorrected Gao Guenie Sample.**

CT Level	Uncorrected		Corrected	
	Volume (mm <sup>3</sup> )	Volume Percent	Volume (mm <sup>3</sup> )	Volume Percent
Low	2242.3	88	2093.0	82
High	292.9	12	456.9	18
Total	2535.2		2549.9	

## 2.5 Conclusion

A simple method to correct for beam hardening has been demonstrated to be applicable to individual CT projections in X-ray transmission data prior to reconstruction, showing application on two systems and protocols. This method is applied post data collection and therefore can be retroactively applied to data previously collected, as long as projection data are preserved. It is possible to obtain calibration data with a single projection using a novel alternating step calibration phantom that is constructed of a material that mimics the attenuation coefficient of the materials that require correction. Various numerical fits may then be examined to determine the best method for linearizing the data for the each situation.

This method allows geoscientists to more reliably explore geomaterials with advanced methods, allowing for fast and non-destructive analysis of the interior of samples without artifacts obscuring the details due to incorrect signal levels. In the next chapter, the application of beam hardening on geomaterials (specifically meteorites) will be explored.

## 2.6 References

- Bourot-Denise, M., Wenmenga, U., & Christophe, M. (1998). The Guenie and Gao chondrites from Burkina Faso: Probably a single shower of stones. *Meteoritics & Planetary Science*, 33(S4), A181-A182.
- Brooks, R.A., & Di Chiro, G. (1976). Beam hardening in x-ray reconstructive tomography. *Phys Med Biol*, 21(3), 390-398.
- Chen, C.Y., Chuang, K.S., Wu, J., Lin, H.R., & Li, M.J. (2001). Beam Hardening Correction for Computed Tomography Images Using a Postreconstruction Method and Equivalent Tissue Concept. *Journal of Digital Imaging*, 14(2), 54-61.
- Herman, G.T. (1979). Correction for beam hardening in computed tomography. *Phys Med Biol*, 24(1), 81.
- Kalender, W.A., Perman, W.H., Vetter, J.R., & Klotz, E. (1986). Evaluation of a prototype dual-energy computed tomographic apparatus. I. Phantom studies. *Med Phys*, 13(3), 334-339.
- Ketcham, R.A., & Carlson, W.D. (2001). Acquisition, optimization and interpretation of X-ray computed tomographic imagery: applications to the geosciences. *Comput. Geosci.*, 27(4), 381-400. doi: 10.1016/s0098-3004(00)00116-3
- Meganck, J.A., Kozloff, K.M., Thornton, M.M., Broski, S.M., & Goldstein, S.A. (2009). Beam hardening artifacts in micro-computed tomography scanning can be reduced by X-ray beam filtration and the resulting images can be used to accurately measure BMD. *Bone*, 45(6), 1104-1116. doi: 10.1016/j.bone.2009.07.078
- So, A., Hsieh, J., Li, J.Y., & Lee, T.Y. (2009). Beam hardening correction in CT myocardial perfusion measurement. *Phys Med Biol*, 54(10), 3031-3050. doi: 10.1088/0031-9155/54/10/005
- Yamada, M., Jinzaki, M., Kuribayashi, S., Imanishi, N., Funato, K., & Aiso, S. (2012). Beam-Hardening Correction for Virtual Monochromatic Imaging of Myocardial Perfusion via Fast-Switching Dual-kVp 64-Slice Computed Tomography. *Circulation Journal*, 76(7), 1799-1801. doi: 10.1253/circj.CJ-12-0463



## Chapter 3

### Co-Authorship Statement

Chapter 3 is an original manuscript that is in preparation for submission to the journal *Meteoritics and Planetary Science*, entitled “Phase recognition and volumetric analysis of meteoritic samples using laboratory micro-computed tomography.” The manuscript is co-authored by David R. Edey, Phil J. A. McCausland, Roberta L. Flemming, and David W. Holdsworth. In my role as a M.Sc. candidate, I participated in designing the study, acquired the images, analyzed all data, performed the statistical analysis, and wrote the manuscript text. Phil McCausland contributed key technical aspects of the methods, aided in the analysis and provided editorial input. Roberta Flemming and David Holdsworth, as the candidate’s supervisors, reviewed the results, gave editorial assistance and provided mentorship. Roberta Flemming also provided key technical expertise for acquisition of microXRD data.

### **3 Phase recognition and volumetric analysis of meteoritic samples using laboratory micro-computed tomography**

#### **3.1 Introduction**

Meteorites provide a range of “returned” samples from small bodies, Mars and the moon, that are otherwise difficult to obtain for laboratory analysis as geological specimens (Hutchison, 2004). Studies of meteoritic samples provide information about materials and processes that were present in our solar system’s protoplanetary disk (Brearley & Jones, 1998) as well as on the formation of planetesimals and planetary bodies (Mittlefehldt et al., 1998).

Meteorites are the next best thing to samples returned from the planetary bodies. Although meteorites do not provide the level of contextual information that a collected sample can provide, they still are geological samples for the bodies from which they originate. The mineralogy within these samples carries information regarding the geochemical, isotopic, thermal and shock metamorphic history of their parent bodies.

Modal mineralogy can also provide useful information regarding the physical properties of the parent bodies, important in predicting impact dynamics and collisional lifetimes of asteroids (Britt et al., 2003). Bulk density can be calculated using the modified Archimedian method (Consolmagno & Britt, 1998) in a non-destructive manner. Combining this with a non-invasive method to determine grain density would provide density and porosity calculations with minimal contamination (Bland et al., 2004).

Current methods of bulk analysis to extract modal mineralogy include Rietveld refinement of powder XRD (pXRD) data (Cloutis et al., 2013; Izawa, Flemming, et al., 2010; Izawa, King, et al., 2010) and calibrated Position Sensitive Detector (PSD) XRD (Bland et al., 2004; Howard et al., 2010). Methods of *in situ* analysis include Energy Dispersive X-rays (EDX)/Scanning Electron Microscopy (SEM) (Hashimoto & Grossman, 1985; Herd et al., 2010; Merouane et al., 2011), petrographic point counting (Buseck, 1977; Stolper & McSween, 1979), and Micro X-ray Diffraction ( $\mu$ XRD) (Flemming, 2007; Izawa, Flemming, et al., 2010; Izawa, King, et al., 2010). These provide useful results and insight into mineralogical composition and structure, but usually require partial destruction of the samples in order to generate data. Because these samples are generally irreplaceable, it would be ideal if analytical techniques could provide similar information without adversely affecting the sample.

Micro-computed X-ray tomography ( $\mu$ CT) can be a powerful tool for analysis of meteorite samples. The ability to visualize internal structure non-destructively has proven to be an effective way of examining samples that are too rare or valuable to cut, or as a means of primary investigation before target areas are chosen for destructive analysis (Arnold et al., 1983; Friedrich, 2008). CT also acts as an archival medium in which samples can be digitally preserved prior to modification or destruction. In addition, the original projection data can subsequently be available for future, more-advanced methods of reconstruction to be retroactively applied. Objects of high radiodensity (e.g. metal, sulphides and oxides in meteorites) in conjunction with the polyenergetic spectrum that is utilized in CT cause artifacts that disrupt the analysis of scan data. Chapter 2 described a method that allows for the reduction or removal of such artifacts, allowing for better

quantitative analysis of reconstructed CT data; in this chapter, this method will be applied to selected meteorite specimens.

Four meteorites of various compositions and characteristics have been chosen for this study. Ozona, found 1929 in Crockett County, Texas, is a highly weathered H6 chondrite (Grady, 2000) with a total of 127.5 kg recovered. Olivine composition has been given as  $Fa_{19}$  (Mason, 1963) but it has been studied little further. Gao-Guenie, an observed fall March 5, 1960 in what is now known as Burkina Faso, is an H5 chondrite. The fall was described as a shower, where the total number of specimens is unknown and where samples are still being found; the largest found sample was 2.5 kg in weight (Grady, 2000). Kamacite and taenite are scattered throughout the bulk material with adjacent chondrule-rich and chondrule-poor areas (Bourot-Denise et al., 1998). Grimsby, a fresh fall observed on September 29, 2009 in Grimsby Ontario, with a total of 215g recovered, is an H4-5 chondrite. It is recorded as having low shock olivine, enstatite, kamacite, and troilite as well as polycrystalline magnesioferrite spinel in the fusion crust, and abundant chondrules and chondrule fragments (McCausland et al., 2010; Weisberg et al., 2010). Finally, Northwest Africa 5480 (NWA 5480), a find in Northwest Africa in 2008, is a coarse-grained olivine diogenite, with a total of 4.91 kg having been recovered (Weisberg et al., 2009).

The first three samples, all being classified as H group ordinary chondrites, share similar properties. Ordinary chondrites are the most abundant type of material in meteorite collections, consisting of 85% of observed falls and characterized by large chondrules (Weisberg et al., 2006). The H group or ‘high iron’ group is defined by high Fe/SiO<sub>2</sub> ratios and relatively low Fe<sup>0</sup>/Fe ratios (Van Schmus & Wood, 1967). The number following the H is a petrographic grade, wherein the H group can range between 3 to 6, with 3 being pristine and 6 having the highest amount of thermal metamorphism (Weisberg et al., 2006) with some authors including a 7, for samples that exhibit partial melting (Brearley & Jones, 1998).

NWA 5480 is an olivine diogenite, a member of the HED clan. HED (howardite, eucrite and diogenite) meteorites have similar O-isotopic compositions and similar Fe/Mn ratios

in their pyroxenes (Weisberg et al., 2006). Similarities in the mineralogical compositions of the HEDs and the apparent surface mineralogy of asteroid 4 Vesta suggest that the HEDs originate from this asteroid (Kelley et al., 2003).

Methods currently employed and trusted by geoscientists will be employed to characterize the mineralogical composition of these meteorites, and results will be compared to micro-CT data to establish the validity and value of CT analysis as a geological sample evaluation and investigation method.

## 3.2 Methods

### 3.2.1 Equipment and software

#### 3.2.1.1 LEO 440 SEM

SEM/EDX examination was carried out with a LEO 440 SEM located at Surface Science Western, The University of Western Ontario, which is equipped with a Quartz XOne EDX system. A 15 kV electron beam was used to obtain back-scattered electron (BSE) images, EDX spectra and X-ray intensity element maps of the surface of Grimsby meteorite samples. The EDX technique can detect all elements above atomic number 5 (carbon to uranium) and it has a minimum detection limit of ~0.5 wt% for most elements. The Quartz XOne system uses full spectral imaging, which allows for live and post-collection data analysis.

#### 3.2.1.2 Micro X-Ray diffraction

Crystal structural information was acquired in situ using a Bruker D8 Discover micro-X-ray Diffractometer (Bruker AXS, Inc., Madison, WI) at the University of Western Ontario (Flemming, 2007). The instrument utilizes  $\theta$ - $\theta$  geometry at 35 kV and 45 mA using a  $\text{CoK}\alpha$  source ( $\lambda = 1.7902 \text{ \AA}$ ). The X-rays are collimated through a göbel mirror parallel optics system and directed through a 300  $\mu\text{m}$  pinhole snout. The X-rays are detected on a Hi-Star 2-dimensional area detector placed 12 cm away from the diffraction surface, and analyzed using General Area Detector Diffraction System (GADDS) software. This results in a resolution of  $0.04^\circ$  in  $2\theta$ , and by using a scanning mode that moves both the detector and source in the same direction simultaneously (omega scan

mode), it is possible to increase the number of lattice planes that satisfy Bragg's law to produce diffracted peaks. This setup allows for single crystals to be analyzed by this essentially powder diffractometer. The two dimensional diffraction data are integrated into a linear diffraction pattern, which can be analyzed using DIFFRAC<sup>plus</sup> Evaluation (EVA) software. This software interface allows phase identification by graphical matching of diffraction patterns to standard patterns in the International Centre for Diffraction Data (ICDD) database.

### 3.2.1.3 Biomedical micro-CT scanners

Two laboratory micro-CT scanners were used in this study, chosen based on specimen size. Both a GE eXplore Locus (Locus) and GE eXplore speCZT (speCZT) were utilized; these instruments are operated by the Robarts Research Institute at The University of Western Ontario. Scans on the Locus were completed at an X-ray tube voltage of 80 kVp and current of 0.45 mA in a 10 cm bore with a 3 cm diameter reconstruction volume. For each scan, 900 views were obtained in 0.4° increments at an exposure time of 4.5 s per frame, with 2 frames captured per view. These scan parameters result in an acquisition duration of approximately 2.75 hours and were reconstructed at 20.2 μm isotropic voxel (volume element) spacing. Scans performed on the speCZT were completed at an X-ray tube voltage of 110 kVp and current of 40 mA using the large focus of the X-ray tube in a 8.89 cm bore. For each scan, 900 views were obtained in 0.4° increments at an exposure time of 16 ms per frame. These scan parameters resulted in an acquisition duration of approximately 5 minutes and are reconstructed at 50 μm isotropic voxel spacing.

### 3.2.1.4 Beam hardening correction

After acquisition of transmission data from the CT scanners, the data is corrected in the method as described in Chapter 2 using an in-house designed correction program and subsequently reconstructed, using the reconstruction system supplied by GE for the corresponding system.

### 3.2.1.5 Olympus STM6 measuring microscope

An Olympus STM6 measuring microscope was utilized for reflected light microscopy. An Olympus UC30 digital camera was attached to provide digital imaging.

## 3.2.2 Sample analysis

### 3.2.2.1 MicroView

MicoView ABA-Fat 2.2.RC5 (MicroView; GE Healthcare, London, ON) was utilized for examining the 3D images produced by the reconstruction software. This software was used to create regions of interest (ROIs) within the sample to determine the average and standard deviation of the radiodensities within these ROIs. An isosurface tool was used to determine the volumes of regions above specified densities; and subsequently subtraction of the regions of higher densities, allowed the volumetric data to be parsed into various sections by their respective radiodensities, as chosen by the histogram of the material, providing the volume of those regions.

### 3.2.2.2 Point counting

A point counting technique was employed on the Gao-Guenie sample cut surface to obtain an estimate of the metallic content. A grid was overlain on a reflected light photomicrograph of the entire cut surface, collected on the Olympus STM6, and at each intersection point it was inspected visually to determine if the underlying material was metallic (being free metal) or not. These counts of metallic composition were then compared to the total number of reference points and converted into percentages and used for compositional analysis.

## 3.2.3 Selection of meteoritic specimens

Four meteorites were chosen for this study on the basis of challenging the ability of micro-CT to examine different compositions and mineralogies: 1) Ozona is a highly weathered H6 ordinary chondrite, with an extremely fine granular matrix chosen to examine the limits of small grain size in CT, as the products of weathering are very fine grained. 2) Gao-Guenie is an H5 ordinary chondrite that has high levels of native metal throughout; this is a material that traditionally inhibits effective examination using CT. 3)

Grimsby is an H4-5 ordinary chondrite, which was mounted in three small epoxy “pucks”. These samples are fine grained and push the limits of the CT scanner resolution. Finally, 4) NWA 5480 is a coarse-grained olivine diogenite. It was chosen to challenge CT in distinguishing between different silicates (olivine, pyroxene).

These four meteorites were chosen to test and stretch the ability of CT, after correction, to differentiate mineralogy within the samples. They represent a wide range of mineralogical compositions, which, along with their unusual shapes, pose challenges to the current state of CT analysis. By implementing semi-empirical beam-hardening correction, and comparing CT with standard geological methods, the aim is to fully examine the capabilities of this method.

### 3.3 Results

#### 3.3.1 Ozona

The examined Ozona sample is a slab with two cut surfaces, measuring 4.5 cm by 3.75 cm (*Figure 3.1*). CT data for Ozona was collected in the speCZT, 6 slices parallel to the XZ plane every 1.3 mm, beginning 650  $\mu\text{m}$  below the surface (*Figure 3.3*) are shown as a representative of the CT volume. A CT slice along the surface is shown in *Figure 3.2*, exhibiting the 2 phases (low and high) that are distinguishable by radiodensity in the CT volumes. Isosurfacing resulted in a total volume of 12768.52  $\text{mm}^3$  for the sample, and a <1% volume/volume (v/v) content for the high-density phase. Calculated volumes and volumetric percentages are summarized in *Table 3.1*.

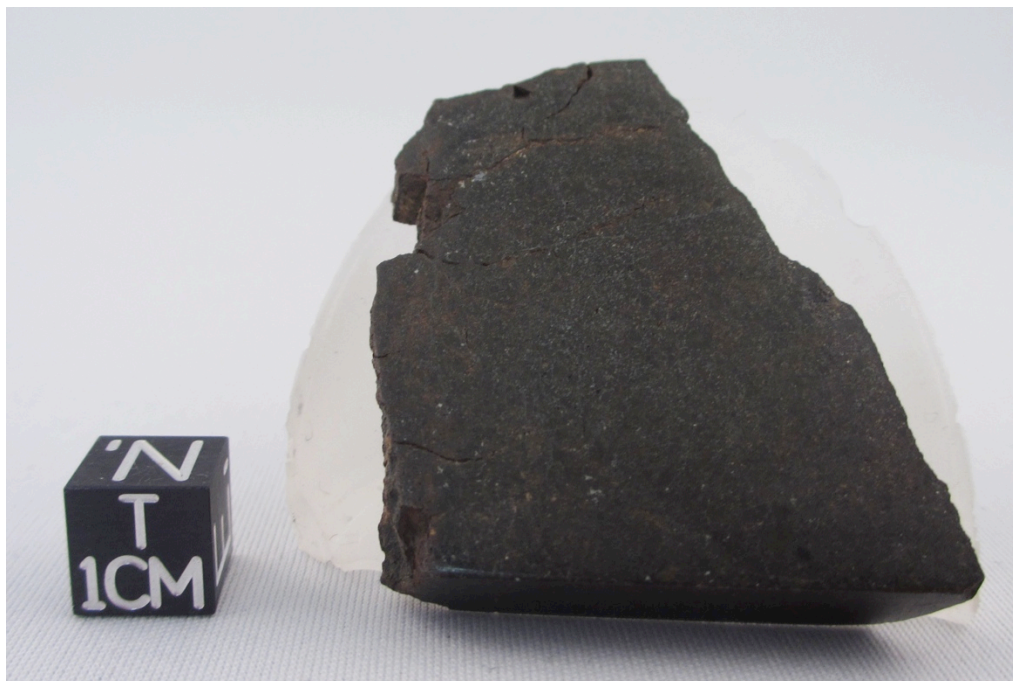


**Figure 3.1 - Photo of Ozona.** Scale cube (1 cm) for size reference.

**Table 3.1 - Volumetric Analysis of Ozona**

CT Level	Volume (mm <sup>3</sup> )	Volume Percent
Low	12759.1	> 99.9
High	9.5	< 0.1
Total	12768.5	

### 3.3.2 Gao-Guenie

Our Gao-Guenie sample is the triangular end cut of a fragment, it measures 1.8 cm by 2.0 cm on two adjacent sides, as seen in *Figure 3.4*. Micrographic point counting was done on Gao-Guenie to determine surface metallic percent (*Figure 3.5*). Veins of sulphides are said to be found in some samples of Gao-Guenie (Bourot-Denise et al., 1998), but were not observed on the surface micrograph or in the CT volume, however their occurrence would be incorporated into the metallic fractionations if they are present. This technique resulted in an estimated metallic content of 14.6% v/v from a total of 5341 points. A surface image of the sample with overlying grid and point counts can be seen in *Figure*



3.5. CT data for Gao-Guenie was collected in the speCZT, 6 slices parallel to the XZ plane every 1.4 mm, beginning 700  $\mu\text{m}$  below the surface are shown as a representative of the volume in *Figure 3.6*. A CT slice along the surface is shown in *Figure 3.5*, exhibiting the two phases (metallic and non-metallic) that are distinguishable by radiodensity in the CT volumes. Isosurfacing these regions resulted in a total volume of  $1247.9 \text{ mm}^3$  for the whole sample and a 14% v/v metallic content. Calculated volumes and volumetric percentages are shown in *Table 3.2*.

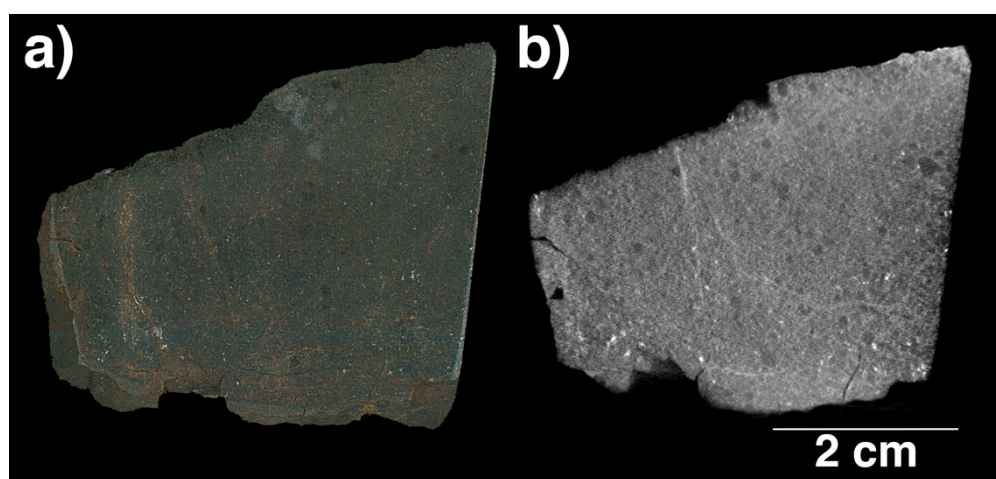


**Figure 3.2 – Photo vs CT scan of Ozona.** a) A photomicrograph, obtained using a standard office scanner and b) a CT slice through the surface collected on the speCZT at 110 kVp and 40 mA.

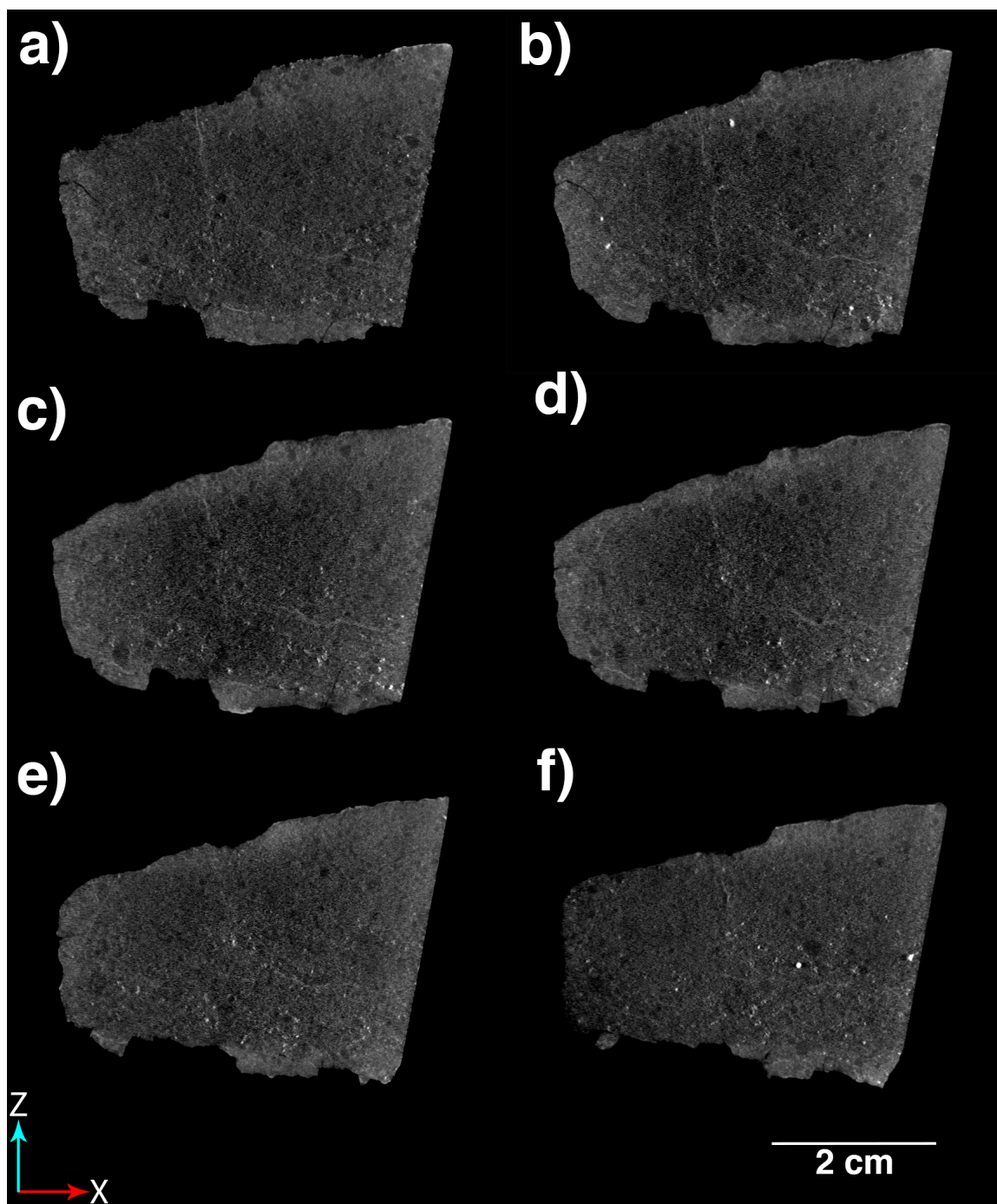


**Figure 3.3 – CT slices through Ozona.** CT slices through Ozona every 1.3 mm, beginning 650  $\mu\text{m}$  below surface collected on the speCZT at 110 kVp and 40 mA.

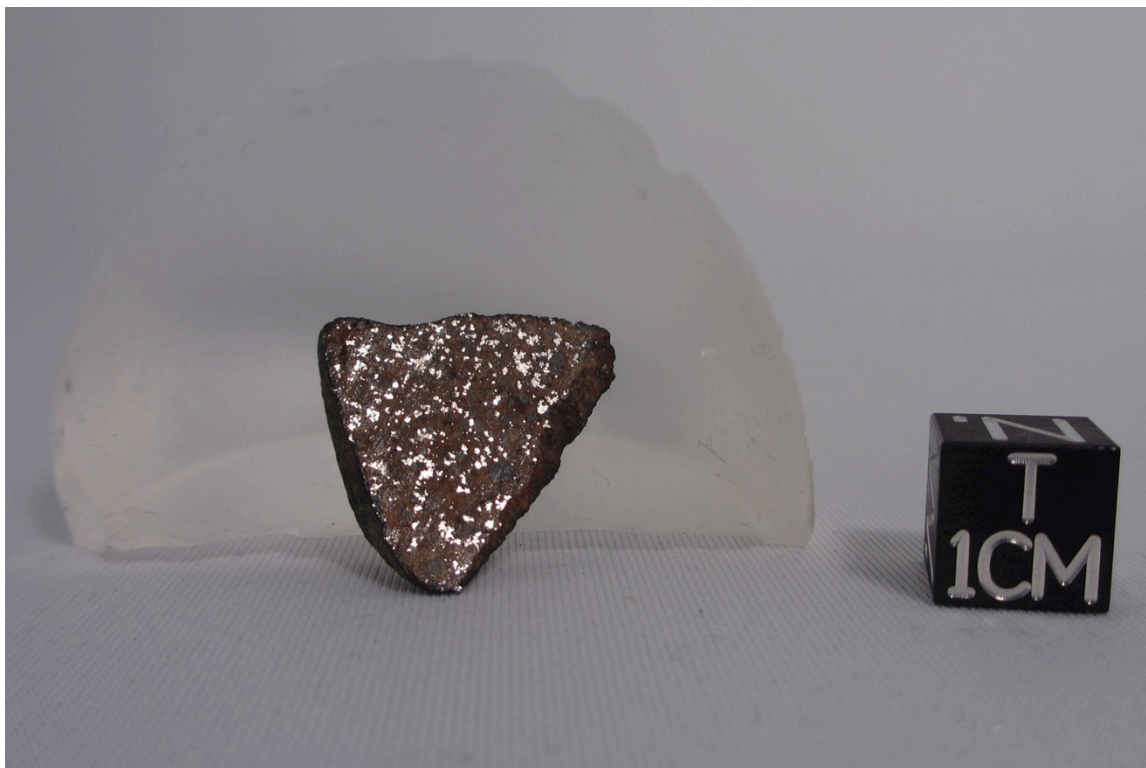


**Figure 3.4 - Photo of Gao-Gueneite.** Scale cube (1 cm) for size reference.

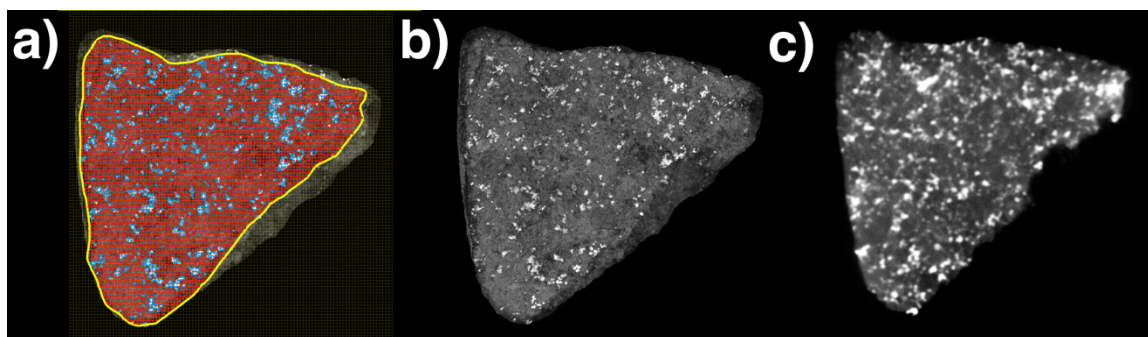


**Figure 3.5 - CT vs. Photo, including point counting grid of Gao-Gueneite.** a) photomicrograph overlain with a point counting grid and results (red = non-metallic; blue = metallic) b) the original photomicrograph obtained using an Olympus STM 30, and c) a CT slice through the surface collected on the speCZT at 110 kVp and 40 mA.

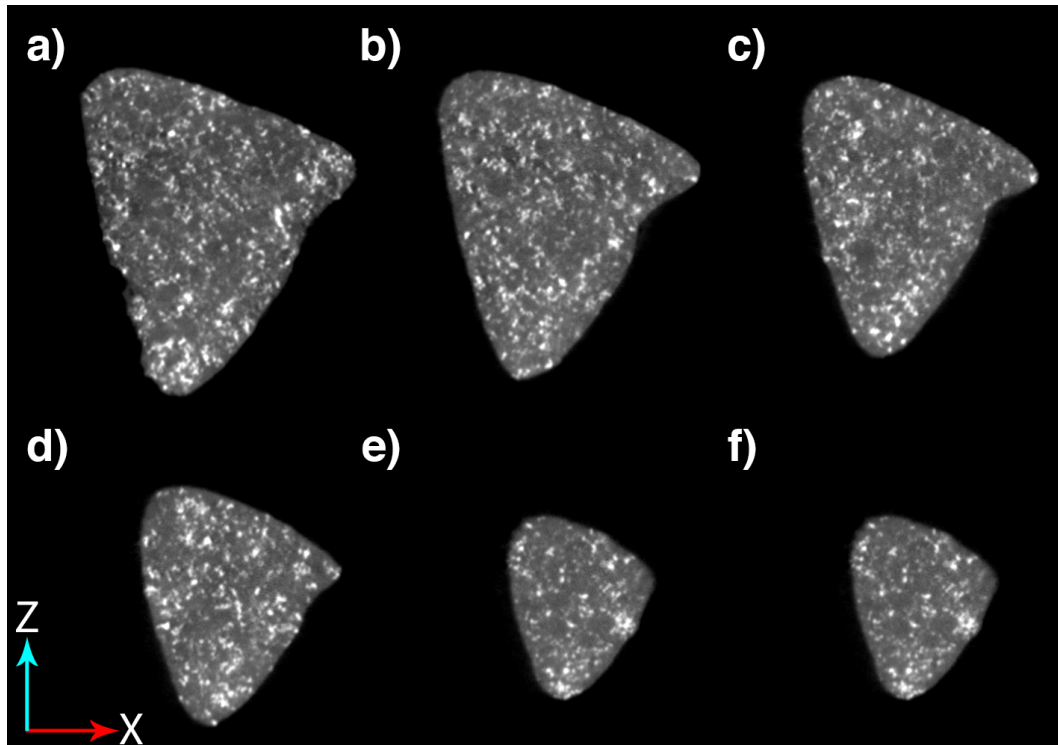


**Figure 3.6 - CT slices through Gao-Guenie.** CT slices through Gao-Guenie every 1.4 mm, beginning 700  $\mu\text{m}$  below surface collected on the specCZT at 110 kVp and 40 mA.

**Table 3.2 - Volumetric Analysis of Gao-Guenie**

CT Level	Volume ( $\text{mm}^3$ )	Volume Percent
Low	1075.5	86
High	172.3	14
Total	1247.8	

### 3.3.3 Grimsby

Grimsby samples are three small samples encased in epoxy pucks: “Peter,” “HP-2” and “Zbyszek.” The samples range from 0.75 – 1 cm in the major axis and 0.3 – 0.5 cm in the minor axis (*Figure 3.7*). SEM and EDX were collected on each of the three Grimsby samples providing high-resolution backscattered electron (BSE) images as well as elemental X-ray maps (*Figure 3.8 - Figure 3.10*). CT data for Grimsby was collected

using the Locus CT scanner. Six slices, parallel to the YZ plane, every 200  $\mu\text{m}$  are shown in *Figure 3.11 - Figure 3.13*, beginning 100  $\mu\text{m}$  below the surface for the three separate samples. A slice through the surface alongside an SEM image of the corresponding surface is shown in *Figure 3.8 - Figure 3.10*. In the CT volume there are two phases (low and high) that are uniquely distinguishable by radiodensity. Isosurfacing resulted in 3% v/v for the high density phase out of a total volume of 22.3  $\text{mm}^3$  for HP-2, 4% v/v high density phase out of 40.0  $\text{mm}^3$  total volume for Zbyszek and 5% v/v high density phase out of 13.3  $\text{mm}^3$  total volume for Peter. Volumes and percentages are shown in *Table 3.3*.

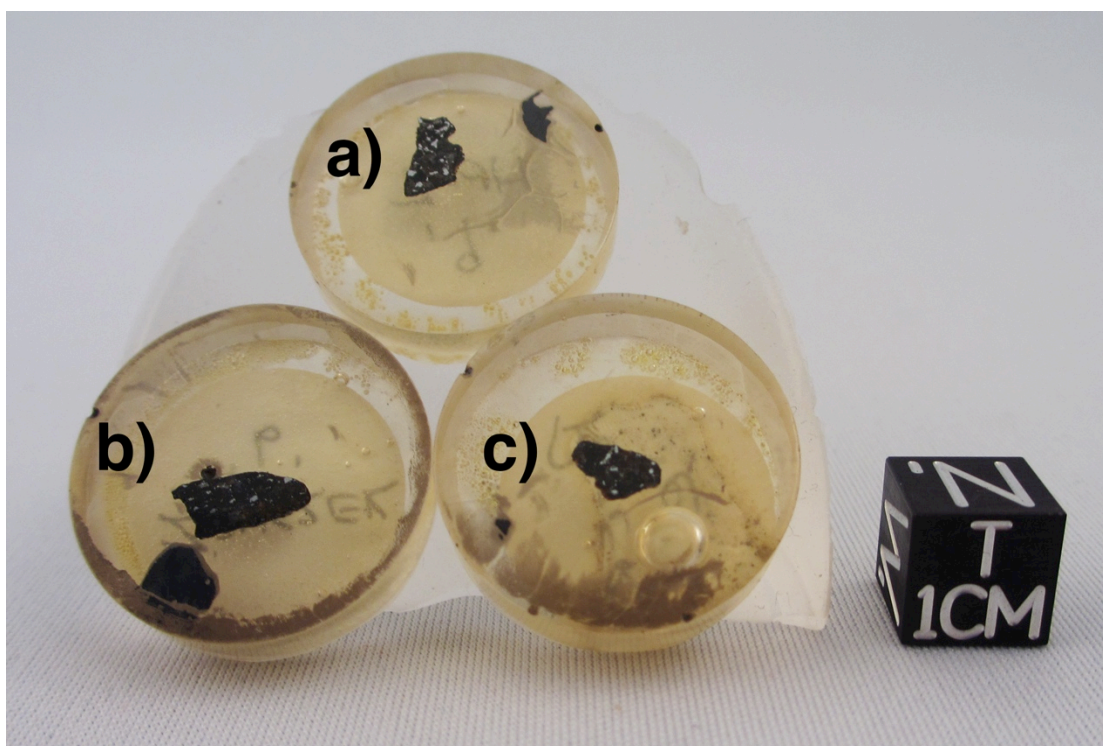


**Figure 3.7 - Photo of Grimsby samples.** Three Grimsby samples a) HP-2, b) Zbyszek and c) Peter. Scale cube (1 cm) for size reference.

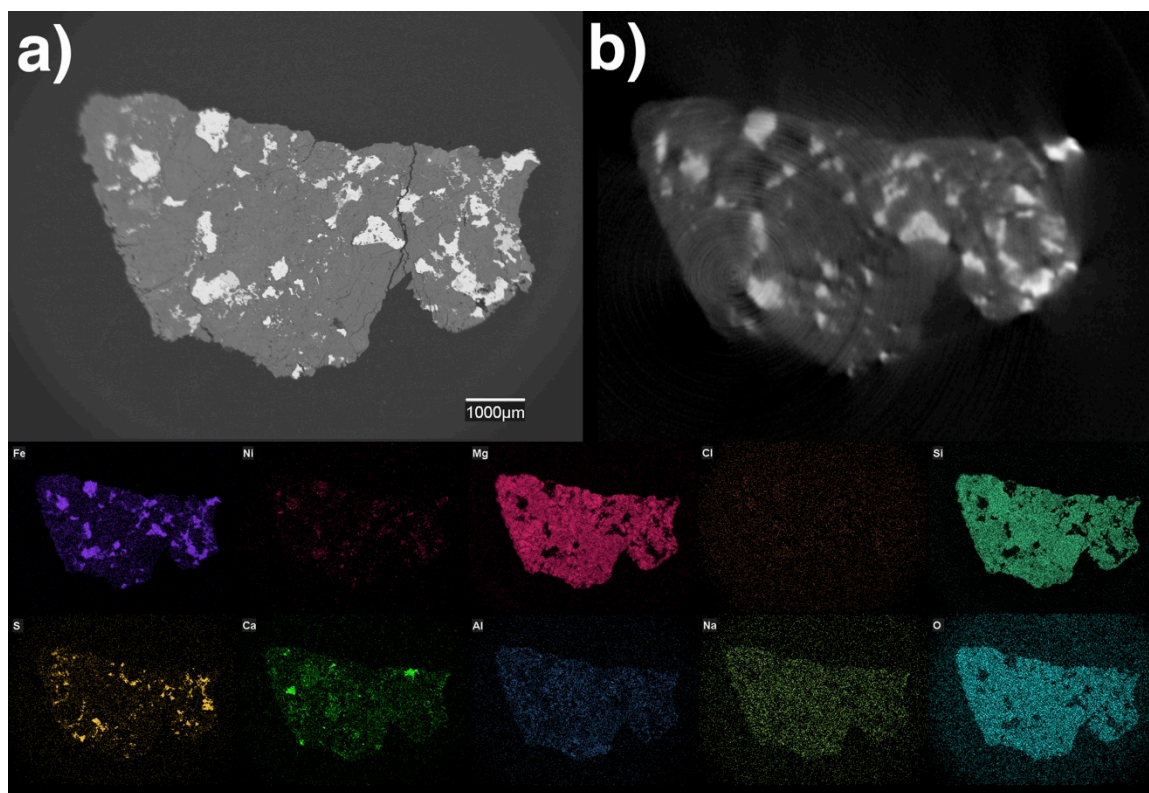


**Figure 3.8 – SEM, EDX and CT images of Grimsby sample HP-2.** a) SEM image of the surface, b) CT slices through the surface collected on the Locus at 80 kVp and 0.45 mA and EDX elemental maps of the surface (below) of Grimsby sample HP-2.

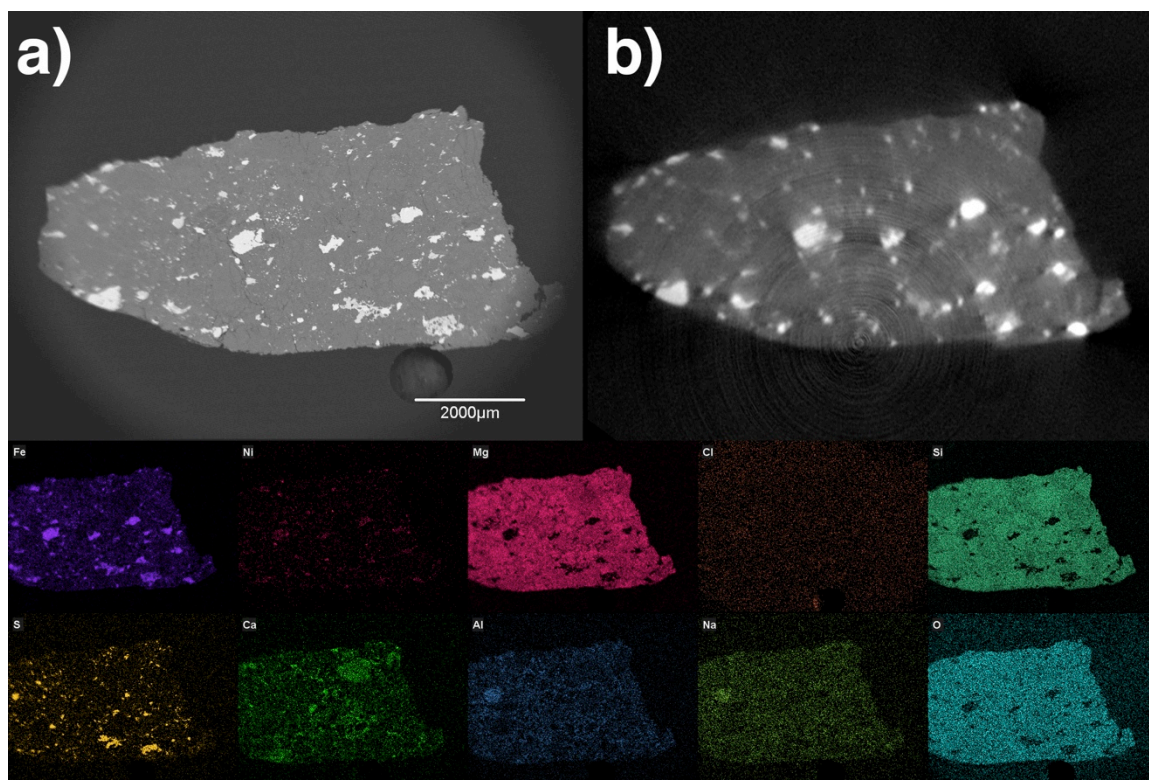


**Figure 3.9 - SEM, EDX and CT images of Grimsby sample Zbyszek.** a) SEM image of the surface, b) CT slices through the surface collected on the Locus at 80 kVp and 0.45 mA and EDX elemental maps of the surface (below) of Grimsby sample Zbyszek.

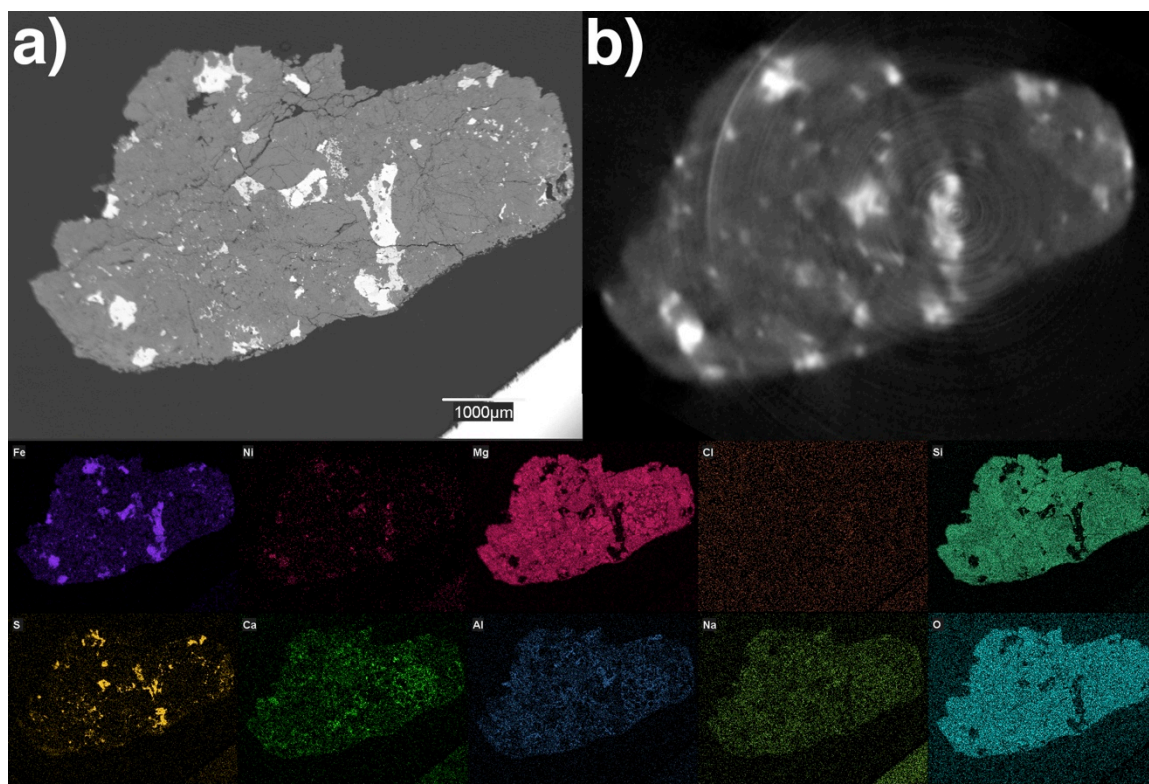


**Figure 3.10 - SEM, EDX and CT images of Grimsby sample Peter.** a) SEM image of the surface, b) CT slices through the surface collected on the Locus at 80 kVp and 0.45 mA and EDX elemental maps of the surface (below) of Grimsby sample Peter.

**Table 3.3 - Volumetric Analysis of Grimsby**

CT Level	HP-2		Zbyszek		Peter	
	Volume (mm <sup>3</sup> )	Volume Percent	Volume (mm <sup>3</sup> )	Volume Percent	Volume (mm <sup>3</sup> )	Volume Percent
Low	21.5	97	29.7	96	12.7	95
High	0.7	3	1.2	4	0.6	5
Total	22.2		39.9		13.3	



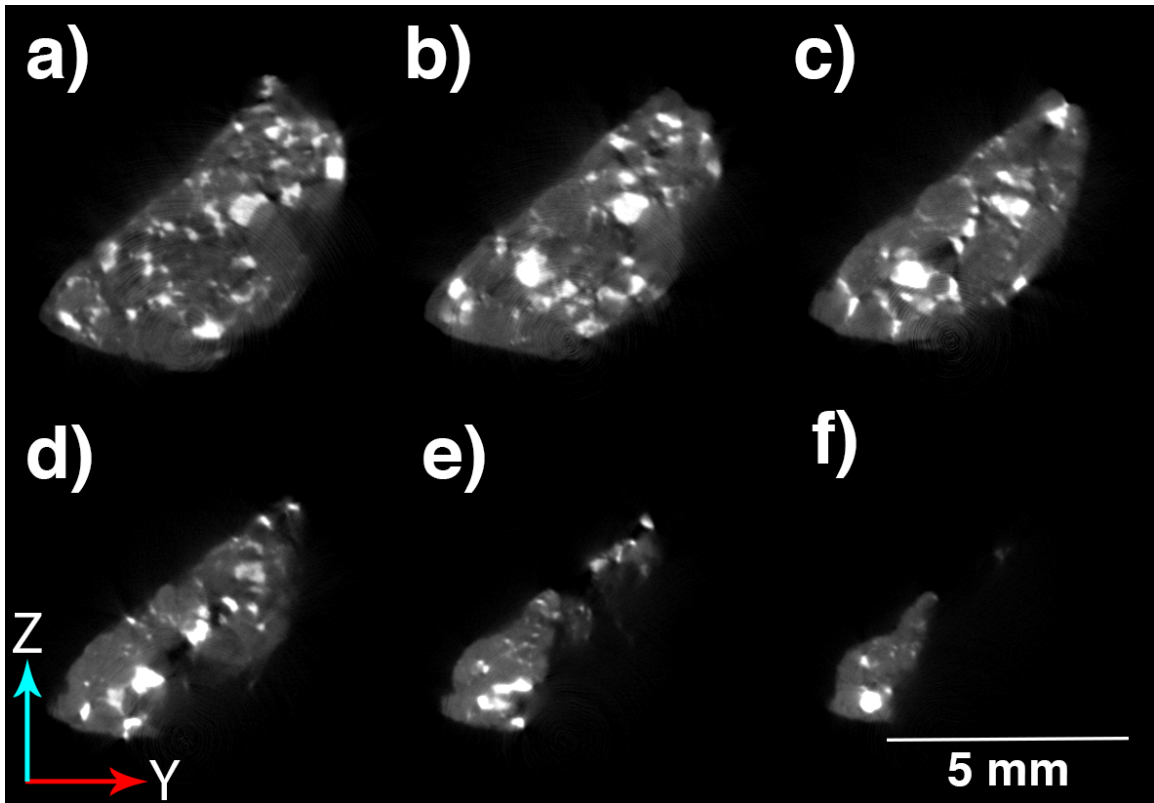


**Figure 3.11 - CT slices through Grimsby sample HP-2.** CT slices through Grimsby sample HP-2 every 200  $\mu\text{m}$  starting 100  $\mu\text{m}$  below surface collected on the Locus at 80 kVp and 0.45 mA.

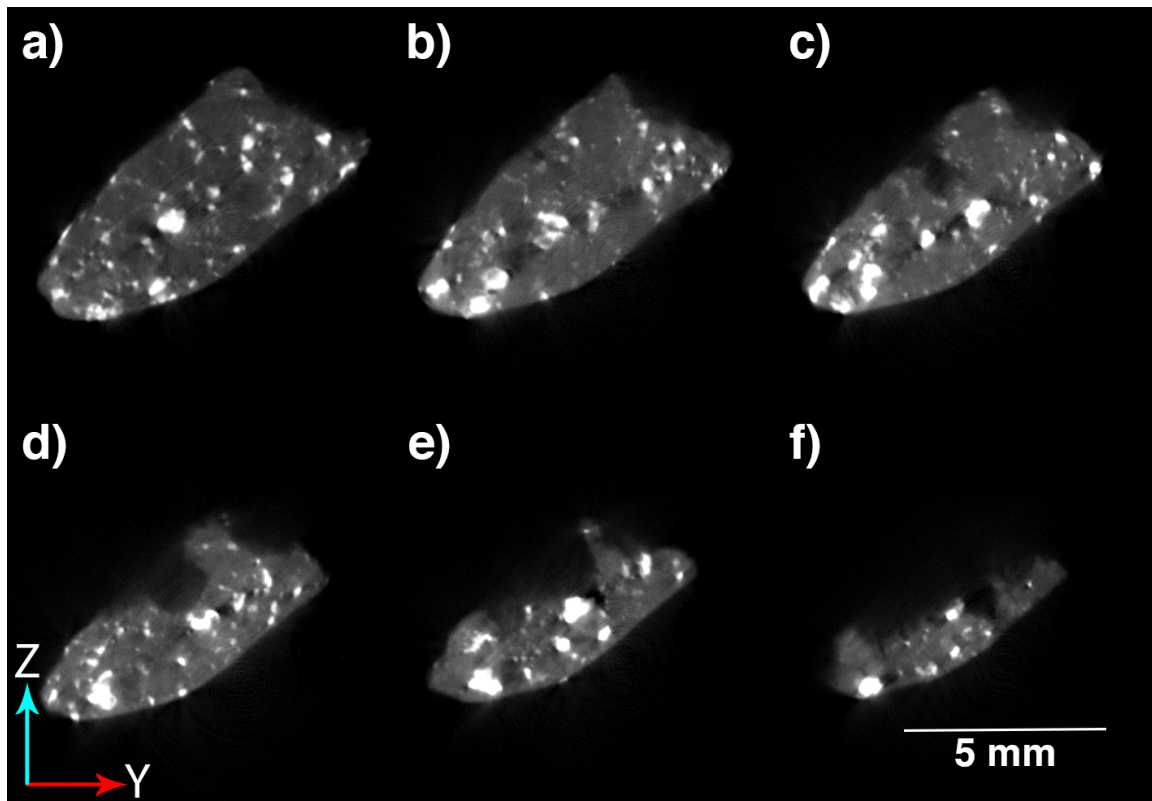


**Figure 3.12 - CT slices through Grimsby sample Zbyszek.** CT slices through Grimsby sample Zbyszek every 200  $\mu\text{m}$  starting 100  $\mu\text{m}$  below surface collected on the Locus at 80 kVp and 0.45 mA.

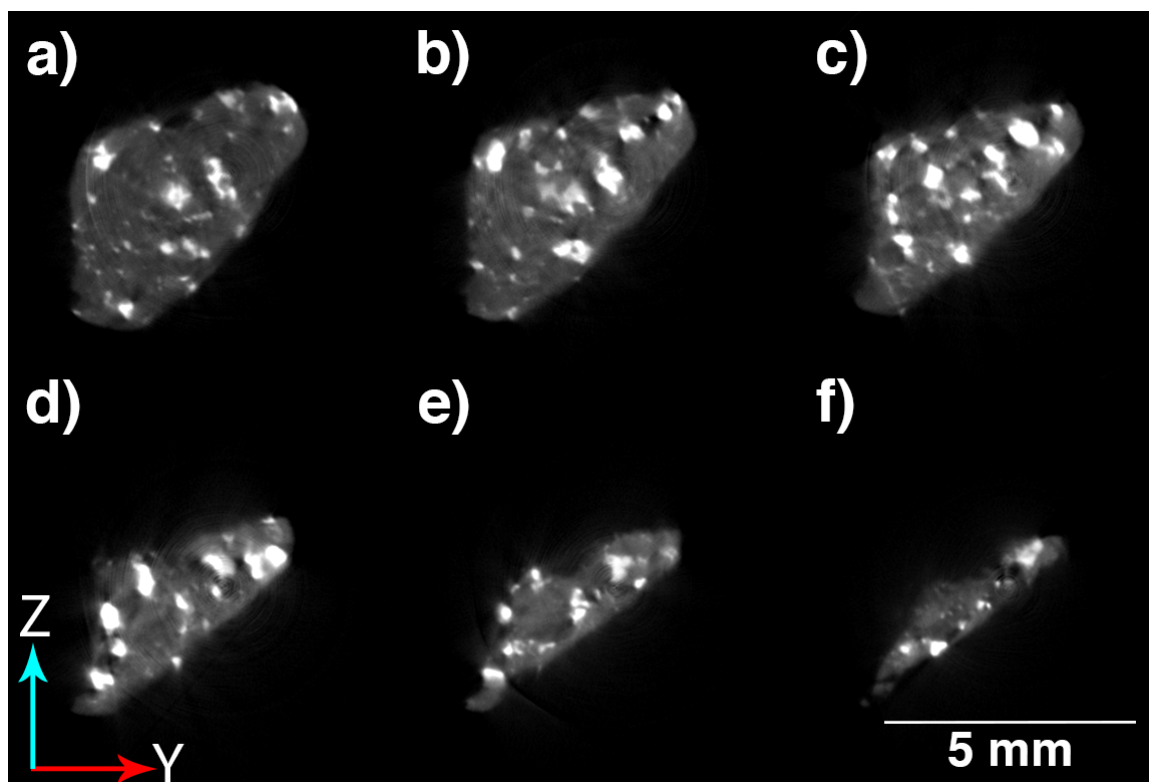


**Figure 3.13 - CT slices through Grimsby sample Peter.** CT slices through Grimsby sample Peter every 200  $\mu\text{m}$  starting 100  $\mu\text{m}$  below surface collected on the Locus at 80 kVp and 0.45 mA.

### 3.3.4 NWA 5480

The NWA 5480 sample is 3 cm by 2 cm on its major and minor axis, as seen in *Figure 3.14*. Diffraction patterns were collected on 10 locations on NWA 5480. Shown in *Figure 3.15*, the data is displayed with associated standard mineral patterns can be seen in *Figure 3.16 - Figure 3.18*. Locations 1 and 2 are structural matches to chromite while locations 3 and 6-10 are structural matches to enstatite, having slightly different compositions than each other. 4 and 5 have the same structure as forsterite, with the same composition at both locations, as summarized in *Table 3.4*. As this is single crystal diffraction, and not all lattice planes satisfy brags law simultaneously, and it is possible to obtain diffraction patterns with missing diffraction peaks in locations where the database has a stick match. CT data for NWA 5480 was collected in the speCZT. Six slices are shown parallel to the XZ plane every 1.50 mm, beginning 0.750 mm below the surface (*Figure 3.19*), as a

representation of the acquired volume. A CT slice along the surface is shown in *Figure 3.15*, showing the three phases (low, medium and high) that are distinguishable by radiodensity in the CT volumes. Isosurfacing the three regions resulted in 1% v/v for the high-density phase and 10% v/v of the medium-density phase out of a total volume of  $2581.82 \text{ mm}^3$ . Calculated volumes and volumetric percentages are shown in *Table 3.5*.



**Figure 3.14 - Photo of NWA 5480.** A coarse-grained olivine diogenite. Scale cube (1 cm) for size reference.

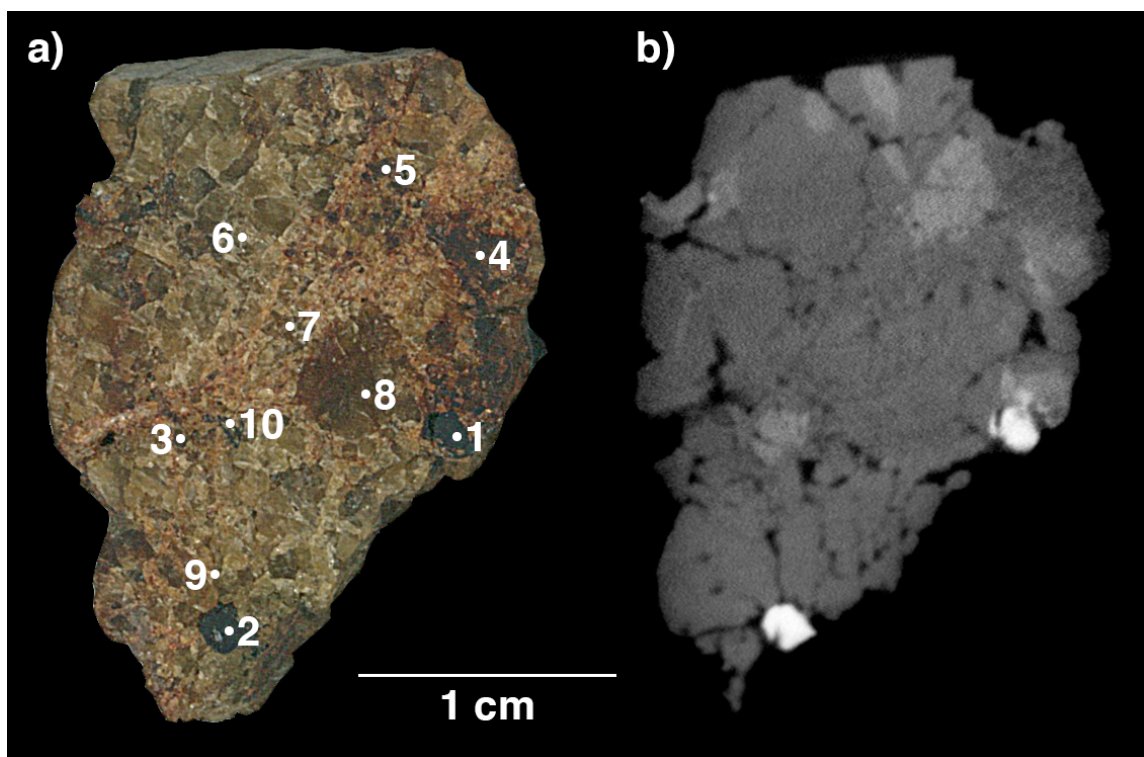


**Figure 3.15 - Photo vs. CT scan, including  $\mu$ XRD locations on NWA 5480.** a) photomicrograph, obtained using a standard office scanner, indicating locations that  $\mu$ XRD were performed, and b) a CT slice through the surface collected on the speCZT at 110 kVp and 40 mA.

**Table 3.4 - Mineral Phases in NWA 5480 by  $\mu$ XRD**

Point	Main Mineral Phase	ICDD Reference
1	Chromite	01-088-1176
2	Chromite	01-088-1176
3	Enstatite, ferroan	01-088-1916
4	Forsterite, ferroan	01-087-0619
5	Forsterite, ferroan	01-087-0619
6	Enstatite, ferroan	01-088-1913
7	Enstatite, ferroan	01-088-1913
8	Enstatite, ferroan	01-088-1913
9	Enstatite, ferroan	01-088-1916
10	Enstatite, ferroan	01-088-1913

**Table 3.5 - Volumetric Analysis of NWA 5480**

CT Level	Volume (mm <sup>3</sup> )	Volume Percent
Low	2307.7	89
Medium	255.0	10
High	19.1	1
Total	2581.8	

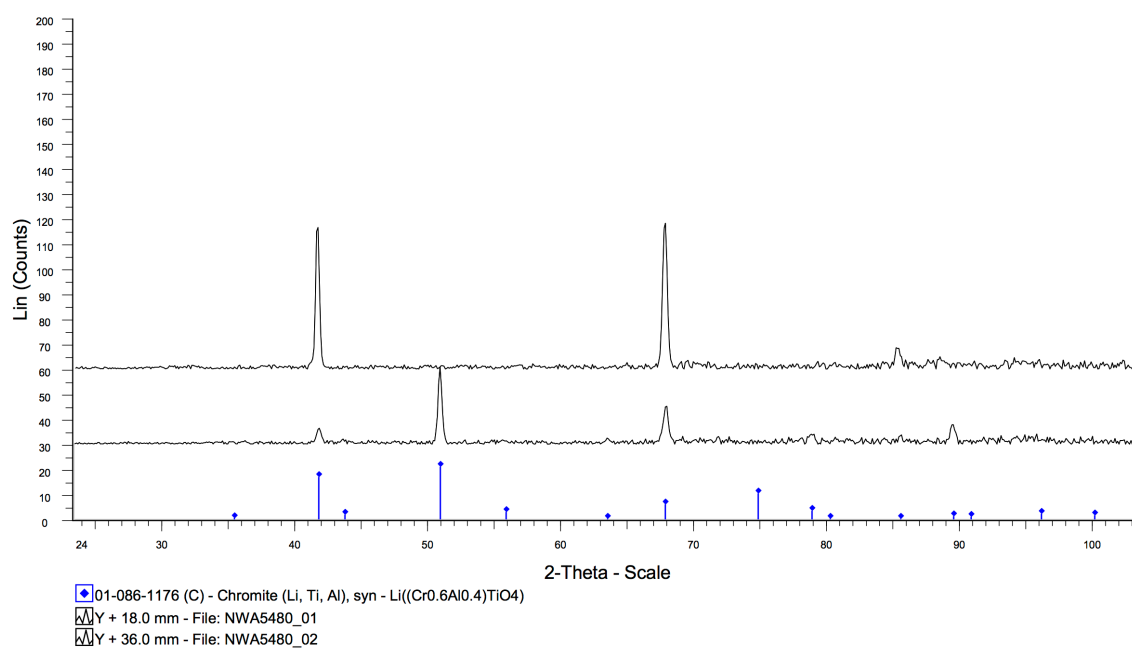


**Figure 3.16 -  $\mu$ XRD Diffraction pattern at locations 1 and 2.** Diffraction pattern obtained at both locations 1 and 2 with a International Centre for Diffraction Data (ICDD) stick pattern for chromite, indicating diffraction match found.

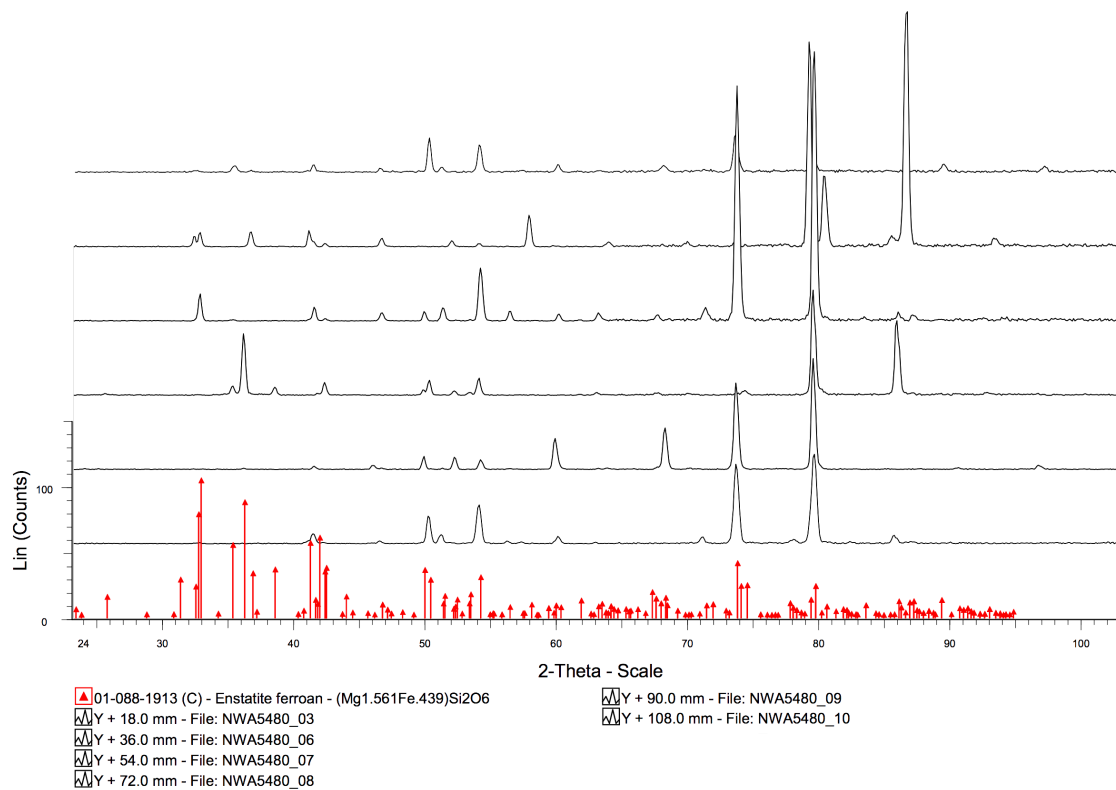


**Figure 3.17 -  $\mu$ XRD Diffraction pattern at locations 3 and 6 - 10.** Diffraction pattern obtained at both locations 3 and 6 - 10 with a ICDD stick pattern for enstatite, indicating diffraction match found.

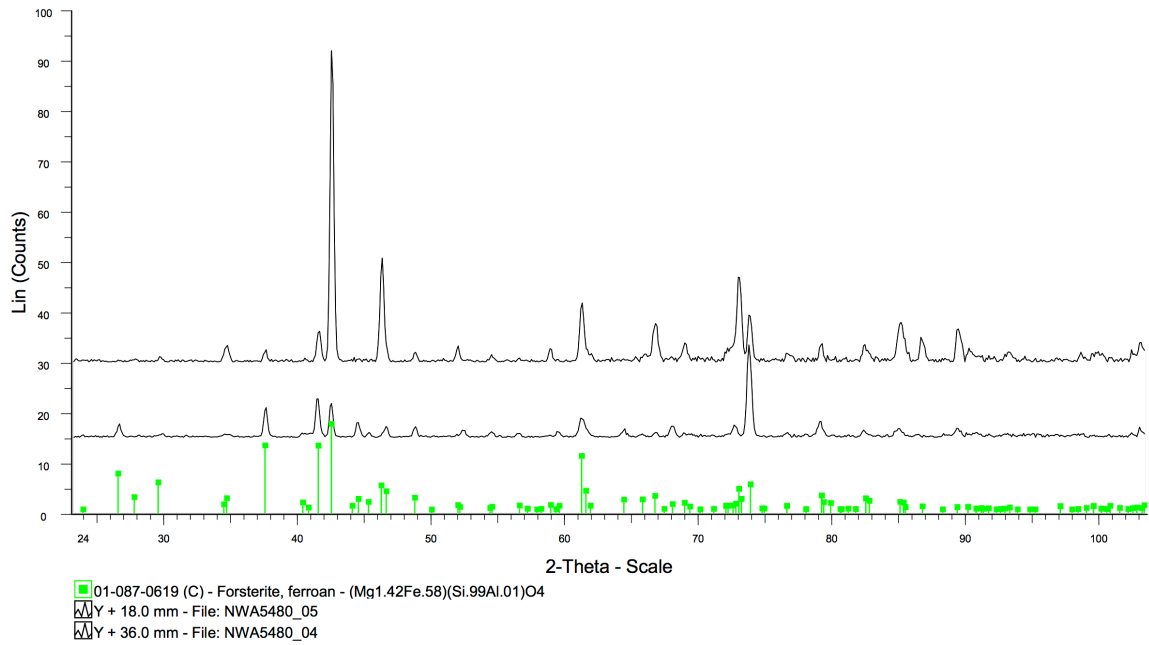


**Figure 3.18 -  $\mu$ XRD Diffraction pattern at locations 4 and 5.** Diffraction pattern obtained at both locations 4 and 5 with a ICDD stick pattern for forsterite, indicating diffraction match found.



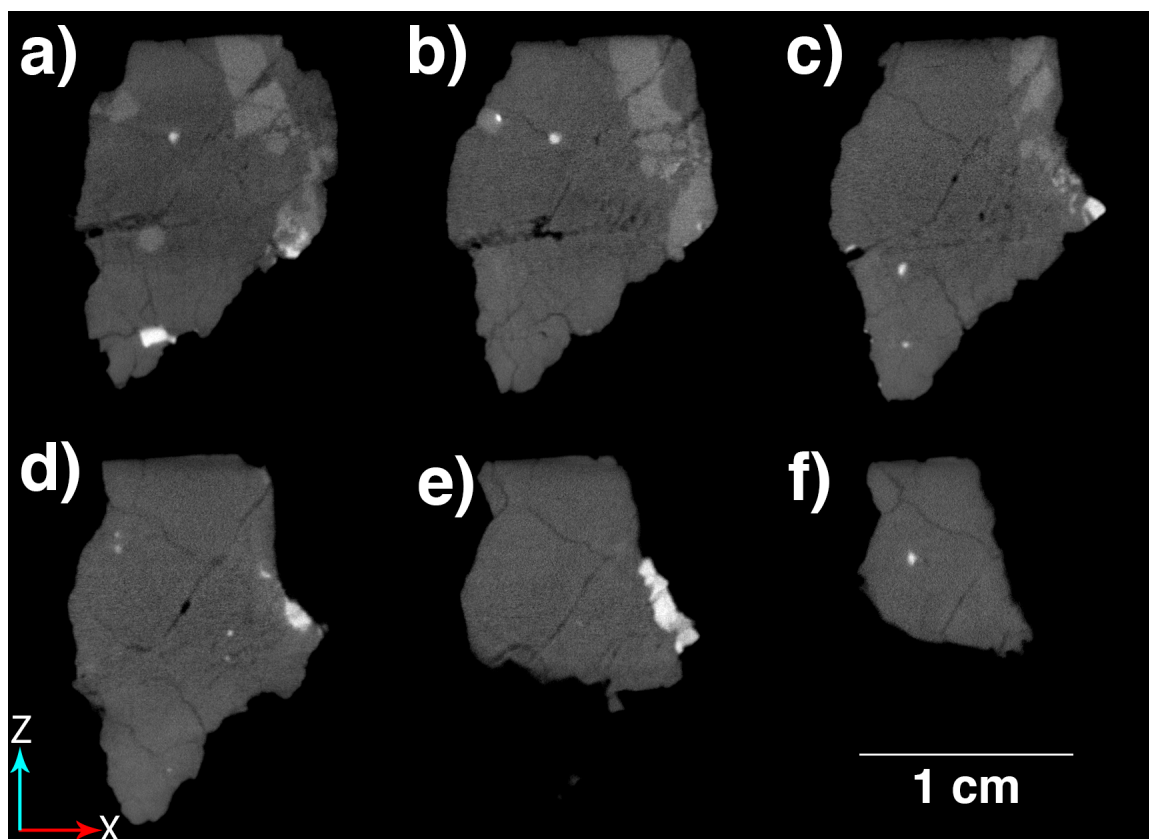


**Figure 3.19 - CT slices through NWA 5480.** CT slices through NWA 5480 every 1.50 mm starting 0.75 mm below surface collected on the speCZT at 110 kVp and 40 mA.

## 3.4 Discussion

### 3.4.1 Ozona

Ozona was a difficult sample from which to distinguish unambiguous information via CT analysis, and is an example of the downfalls of CT in geo-material analysis. Its fine grained nature and similar radiodensity of the different phases challenge the limits of CT. Although some volumetric information was obtained regarding the sample on the whole, and the few areas of high density, it was hard to provide quantitative information. The CT volume still provides high-caliber qualitative images though the entire sample (*Figure 3.3*), showing, high density, oxide-rich veins can be qualitatively observed by CT but quantification was difficult because the veins had indistinct boundaries at the voxel scale and often seemed to be approximately only one or two voxels wide alongside a few

bright inclusions. Overall, information regarding much of the mineralogy is difficult to obtain.

### 3.4.2 Gao-Guenie

Gao-Guenie has a particularly high metallic content that, especially prior to beam hardening correction, obfuscates the CT analysis by causing cupping artifacts in the metallic and sulphide locations and streaking artifacts in the surrounding matrix (Wilting, 1999). After correction, it becomes easier to separate the phases within the sample. Due to the noise of the volume being larger than the average reported radiodensity between the two phases it is not possible to differentiate different silicate constituents or the chondrules from within the fine-grained matrix or metallic phases from the sulphides. The high metallic and sulphide content has a radiodensity that is appreciably different from the surroundings, making those phases easy to separate. Isosurfacing the meteorite to create a surface mesh of the two constituents, metal-sulphide and silicate matrix, using the CT scan data resulted in a metallic content of 14% v/v over the entirety of the sample, while point counting estimated a 14.6% v/v. These values are remarkably similar. We assume this difference arises from two factors. The point counting technique provides a highly accurate estimate of the composition (Van der Plas & Tobi, 1965), but it assumes that the surface is representative of the whole body. Comparatively, although CT analyzes the whole volume, its resolution is a hard limit, and due to the partial volume effect as a result of that resolution, can only provide accuracies on the order of magnitude of that resolution (Ketcham & Carlson, 2001). CT volume calculations aligned with traditional point counting techniques used to estimate the metallic percentages by using the surface mineralogy. Although it was necessary to cut the sample for comparison, future analysis of metallic content could be done using CT without cutting, thus making the metallic content analysis by CT much more powerful than that of a point counting grid. The voxel resolution is a hard limit for the size of objects (like metal blebs) for which one could estimate the volume. It works in this sample because the metal and sulphide blebs are typically larger than the voxel size, easily satisfying the Nyquist sampling criteria.

### 3.4.3 Grimsby

Grimsby is a series of very small samples encased in epoxy pucks. Although it was scanned on a higher resolution scanner than the other samples in this study, this scanner also suffers from a higher level of reconstruction artifacts; the most notable being ring artifacts (Prell et al., 2009) which can be seen by the series of concentric rings in *Figure 3.8 - Figure 3.9*. The combination of the small sample sizes and the reconstruction artifacts limits the capabilities of CT in these samples. However, their small physical size and relatively small grain size requires that they be scanned on a scanner of this resolution. Even with such limitations it is possible to distinguish two different phases of the sample using  $\mu$ CT. However, these two densities contain more than one mineralogical phase.

EDX element maps (*Figure 3.8 - Figure 3.10*) indicate that the regions of high radiodensity in CT all contain elevated amounts of iron, as kamacite (FeNi alloy) or troilite (FeS). This iron is associated with high levels of sulfur in some locations (troilite), reducing the iron content when sulfur is present. Iron is associated with small amounts of nickel in other locations (kamacite), but this association is indistinguishable in the CT volumes. The areas of low radiodensity in CT are mostly uniform by EDX, but show varying levels of calcium in specific regions, where high calcium is not associated with sulphide or silicate. It is associated with the element phosphorus (which has not been mapped), in the mineral apatite,  $\text{Ca}_5(\text{PO}_4)_3\text{F}$ , which has been reported in Grimsby (McCausland et al., 2010). The calcium variation is not distinguishable in the CT volumes and is grouped with the low-density volumes.

SEM surface scans (BSE images) share a large amount of similarity to the surface slices through the CT volumes (*Figure 3.8 - Figure 3.10*), where areas of high radiodensity in CT also are shown to have high electron density. In the SEM images, it is possible to distinguish areas that have high sulfur content (troilite) from those of higher iron content (kamacite), in contrast to CT where those areas are indistinguishable. Additionally, resolution and contrast of the SEM images are much higher than that of CT, but SEM only provides surface information, whereas CT can provide information about the entire object, while still intact.

Using CT it is still possible to give volumetric information about the two regions (high and low iron) by correlating this EDX information on the surface to the CT slice through the surface, it is then possible to extend that information into the whole CT volume. Total volumes range from 13.3 to 40.0 mm<sup>3</sup> with 3.4 to 4.8% v/v of areas of high iron content for the three samples (*Table 3.5*).

#### 3.4.4 NWA 5480

Utilizing CT, it is possible to distinguish the separate mineral phases in our NWA 5480 sample, due to its coarse-grained nature and a high difference between radiodensities of the different phases. Using a CT slice through the surface it is possible to predict locations that should have similar mineralogy, and thus similar diffraction patterns. From a CT scan of the object prior to  $\mu$ XRD, ten locations were chosen where different mineral identifications were predicted.  $\mu$ XRD analysis identified the phases enstatite, forsterite and chromite, which correspond to the NWA 5480 mineralogy described in the literature (Irving et al., 2009). Two locations, 3 and 10, were expected to have matching diffraction patterns to locations 4 and 5 (forsterite) however it resulted in diffraction patterns that matched the mineralogy of the surrounding area (enstatite). This is most likely a result of the partial volume effect (Wilting, 1999), where it is impossible to represent just the surface of the object with 50  $\mu$ m slices. In these locations, it is possible that there is forsterite below the surface, farther than is penetrated by  $\mu$ XRD, which is  $\sim$ 2-50  $\mu$ m, depending on incident diffraction angle and absorptivity of the material (Jenkins & Snyder, 1996), but close enough to the surface for it to appear there in the CT slice volume.

Taking the  $\mu$ XRD data, and correlating it back to the CT volume, we can see that it is possible to separate the mineral phases within NWA 5480 with little difficulty, even to distinguish between the different silicates: enstatite (lower radiodensity) and forsterite (higher radiodensity). Chromite, due to its much higher radiodensity, is easier to separate. These phases exist throughout the volume, as shown in *Figure 3.19*. With these data it is possible to determine the mineralogies on the surface using  $\mu$ XRD and extend that information back to CT volumes to determine the volumetric makeup of NWA 5480. By

referencing *Table 3.5*, the sample of NWA 5480 consists of 1% v/v chromite, 10% v/v forsterite and 89% v/v enstatite.

### 3.4.5 Summary, limitations, and future work

Micro-CT is a powerful tool that continues to benefit geoscientists; it is capable of imaging the interior of meteoritic samples and allows for valuable volumetric data to be obtained in a non-destructive manner, a feat that is difficult or impossible to gain via other methods. The utilization of biomedical  $\mu$ CT scanners shows that these readily available devices are able to provide quality data that can be used to better understand the makeup and mineral composition of meteorites.

Although CT can provide relatively high resolution though a volumetric sample of many meteoritic samples, it does, however, fail to provide all data that can be provided by traditional geologic analysis. All of our samples were relatively small in size, and while this mostly speaks to the size of our CT scanners and the intensity of their X-ray sources, large samples would become difficult to scan on all but the largest and most powerful machines. Additionally, using CT analysis with beam hardening correction makes the determination of interior information possible within these samples.

Further analysis of a wide range of meteorites is underway, and will continue to provide important information that can extend this research. By collecting a vast array of samples and correlating that information back to other methods, it is conceivable that future work could predict mineralogy with CT without the need for additional analysis. It may also be beneficial to collect and obtain a database of CT volumes containing only single crystals, as well as multiple crystals of the same origin; this again would help in the understanding of X-ray computed tomography of all geomaterials, including meteorites.

## 3.5 Conclusion

Micro-computed tomography can be a valuable tool for the analysis of meteorites. It provides a quick, non-destructive method of seeing inside the samples, providing high quality images for qualitative analysis. It also can provide quantitative volumetric measurements within certain limitations. It is possible to use these devices for coarse-

grained samples to calculate mineral volume content with high accuracy in a quick and easy manner, as in HED meteorites, and using the same methods can provide metallic content measurements on par with traditional techniques. It is easier to provide this information on larger samples with grain sizes that are large (encapsulating 2-3 voxels) compared to the resolution of the reconstruction, but even small samples with small grains, CT can provide useful information regarding the volume composition, albeit limited in comparison to ideal conditions, provided the phases have large enough separation in their respective radiodensity. Samples with smaller grain size can be analyzed using scanners with higher resolution, but the difficulties in producing such high-resolution volumes needs to be taken into account. Even in samples with both small grain sizes and similar radiodensity confounding quantitative volumetric analysis, it is still possible to provide useful contextual analysis that is unparalleled by other imaging techniques.

### 3.6 References

- Arnold, J.R., Testa, J.P., Friedman, P.J., & Kambic, G.X. (1983). Computed Tomographic Analysis of Meteorite Inclusions. *Science*, 219(4583), 383-384.
- Bland, P.A., Cressey, G., & Menzies, O.N. (2004). Modal mineralogy of carbonaceous chondrites by X-ray diffraction and Mössbauer spectroscopy. *Meteoritics & Planetary Science*, 39(1), 3-16.
- Bourot-Denise, M., Wenmenga, U., & Christophe, M. (1998). The Guenie and Gao chondrites from Burkina Faso: Probably a single shower of stones. *Meteoritics & Planetary Science*, 33(S4), A181-A182.
- Brearley, A.J., & Jones, R.H. (1998). Chondritic meteorites. *Reviews in Mineralogy and Geochemistry*, 36(1), 3.1-3.398.
- Britt, D., Yeomans, D., Housen, K., & Consolmagno, G. (2003). Asteroid density, porosity, and structure.
- Buseck, P.R. (1977). Pallasite meteorites—mineralogy, petrology and geochemistry. *Geochimica et Cosmochimica Acta*, 41(6), 711-740.
- Cloutis, E., Izawa, M., Pompilio, L., Reddy, V., Hiesinger, H., Nathues, A., . . . Bell III, J. (2013). Spectral reflectance properties of HED meteorites+ CM2 carbonaceous chondrites: Comparison to HED grain size and compositional variations and implications for the nature of low-albedo features on Asteroid 4 Vesta. *Icarus*.
- Consolmagno, G., & Britt, D. (1998). The density and porosity of meteorites from the Vatican collection. *Meteoritics & Planetary Science*, 33(6), 1231-1241.
- Flemming, R.L. (2007). Micro X-ray diffraction (uXRD): a versatile technique for characterization of Earth and planetary materials. *Canadian Journal of Earth Sciences*, 44(9), 1333-1346.
- Friedrich, J.M. (2008). Quantitative methods for three-dimensional comparison and petrographic description of chondrites. *Computers & Geosciences*, 34(12), 1926-1935. doi: <http://dx.doi.org/10.1016/j.cageo.2008.05.001>
- Grady, M.M. (2000). *Catalogue of meteorites*: Cambridge University Press.
- Hashimoto, A., & Grossman, L. (1985). *SEM-petrography of Allende fine-grained inclusions*. Paper presented at the Lunar and Planetary Institute Science Conference Abstracts.
- Herd, C., Stern, R., Walton, E., Li, J., & Bibby, C. (2010). *TEM and SEM-CL analysis of baddeleyite in NWA 3171: Geochronological implications for Martian meteorites*. Paper presented at the Lunar and Planetary Institute Science Conference Abstracts.

- Howard, K., Benedix, G., Bland, P., & Cressey, G. (2010). Modal mineralogy of CV3 chondrites by X-ray diffraction (PSD-XRD). *Geochimica et Cosmochimica Acta*, 74(17), 5084-5097.
- Hutchison, R. (2004). *Meteorites: A petrologic, chemical, and isotopic synthesis* (Vol. 2): Cambridge University Press.
- Irving, A.J., Bunch, T.E., Kuehner, S.M., Wittke, J.H., & D. Rumble, I. (2009). *Peridotites Related To Avesta: Deep Crustal Igneous Cumulates And Mantle Samples*. Paper presented at the LPSC 2009, The Woodlands, TX.
- Izawa, M., Flemming, R.L., King, P.L., Peterson, R.C., & McCausland, P.J. (2010). Mineralogical and spectroscopic investigation of the Tagish Lake carbonaceous chondrite by X-ray diffraction and infrared reflectance spectroscopy. *Meteoritics & Planetary Science*, 45(4), 675-698.
- Izawa, M., King, P., Flemming, R., Peterson, R., & McCausland, P. (2010). Mineralogical and spectroscopic investigation of enstatite chondrites by X-ray diffraction and infrared reflectance spectroscopy. *Journal of Geophysical Research: Planets* (1991–2012), 115(E7).
- Jenkins, R., & Snyder, R. (1996). *Introduction to X-ray powder diffractometry*: Wiley (New York).
- Kelley, M.S., Vilas, F., Gaffey, M.J., & Abell, P.A. (2003). Quantified mineralogical evidence for a common origin of 1929 Kollaa with 4 Vesta and the HED meteorites. *Icarus*, 165(1), 215-218.
- Ketcham, R.A., & Carlson, W.D. (2001). Acquisition, optimization and interpretation of X-ray computed tomographic imagery: applications to the geosciences. *Comput. Geosci.*, 27(4), 381-400. doi: 10.1016/s0098-3004(00)00116-3
- Mason, B. (1963). Olivine composition in chondrites. *Geochimica et Cosmochimica Acta*, 27(10), 1011-1023.
- McCausland, P., Brown, P., Hildebrand, A., Flemming, R., Barker, I., Moser, D., . . . Edwards, W. (2010). *Fall of the Grimsby H5 chondrite*. Paper presented at the Lunar and Planetary Institute Science Conference Abstracts, The Woodlands, Texas.
- Merouane, S., Djouadi, Z., Brunetto, R., Borg, J., & Dumas, P. (2011). *Analyses of a few fragments from the Paris meteorite through SEM/EDX, micro-FTIR and micro-Raman spectroscopies*. Paper presented at the EPSC-DPS Joint Meeting 2011.
- Mittlefehldt, D.W., McCoy, T.J., Goodrich, C.A., & Kracher, A. (1998). Non-chondritic meteorites from asteroidal bodies. *Reviews in Mineralogy and Geochemistry*, 36(1), 4.1-4.195.



- Prell, D., Kyriakou, Y., & Kalender, W.A. (2009). Comparison of ring artifact correction methods for flat-detector CT. *Phys Med Biol*, 54(12), 3881-3895. doi: 10.1088/0031-9155/54/12/018
- Stolper, E., & McSween, H.Y. (1979). Petrology and origin of the shergottite meteorites. *Geochimica et Cosmochimica Acta*, 43(9), 1475-1498.
- Van der Plas, L., & Tobi, A. (1965). A chart for judging the reliability of point counting results. *American Journal of Science*, 263(1), 87-90.
- Van Schmus, W., & Wood, J.A. (1967). A chemical-petrologic classification for the chondritic meteorites. *Geochimica et Cosmochimica Acta*, 31(5), 747-765.
- Weisberg, M.K., McCoy, T.J., & Krot, A.N. (2006). Systematics and evaluation of meteorite classification. *Meteorites and the early solar system II*, 1, 19-52.
- Weisberg, M.K., Smith, C., Benedix, G., Folco, L., Righter, K., Zipfel, J., . . . Aoudjehane, H.C. (2009). The Meteoritical Bulletin, No. 95. *Meteoritics & Planetary Science*, 44(3), 429-462.
- Weisberg, M.K., Smith, C., Benedix, G., Herd, C.D., Righter, K., Haack, H., . . . Grossman, J.N. (2010). The Meteoritical Bulletin, No. 97. *Meteoritics & Planetary Science*, 45(3), 449-493.
- Wilting, J. (1999). Technical aspects of spiral CT. *medicamundi*, 43, 34-43.

## Chapter 4

### 4 Conclusions and Future Directions

#### 4.1 Summary of Results

Micro-computed tomography is a valuable tool for imaging the insides of opaque materials with increasing applications for geoscientists and meteoriticists. Although the application of  $\mu$ CT is becoming more prevalent in geoscientific research (Baker et al., 2012) this is mostly being performed on either highly-specialized and rare industrial scanners (Benedix et al., 2008; Cunningham & Sukop, 2011; Cunningham et al., 2009; Goergen & Whitney, 2012; Hawkins et al., 2007; Hirose & Hayman, 2008), or on synchrotron-source CT scanners (Ebel & Rivers, 2007; Ebel et al., 2008; Friedrich et al., 2008; Hirano et al., 1990). While these techniques provide exceptional results, biomedical CT scanners can provide ample resolution and analysis quality comparable to many traditional quantitative analysis methods, as well as additional qualitative analysis. Biomedical CT scanners have a much larger installed base throughout the world, provide easier access to and lower costs for analysis. It is, however, not without its flaws. As discussed above, the lower peak energy utilized in these biomedical scanners exacerbates the phenomenon of beam hardening, or the preferential absorption of lower X-ray energies, resulting in characteristic artifacts in the reconstruction volumes.

By implementing a semi-empirical correction to beam hardening it is possible to correct for these artifacts in a reliable and repeatable manner. This method incorporates empirical measurements about the non-linear response of X-ray attenuation within the CT scanner as a result of the heterogeneity of the X-ray spectrum and applies a pixel-by-pixel correction to the projection radiographs prior to reconstruction. This algorithm effectively re-linearizes the response of the material without interfering with collection or reconstruction of data. By choosing to calibrate using a novel calibration phantom, the non-linearity of the system can be analyzed using a single radiograph projection and allows for correction of a wide range of materials, provided that careful material selection is used when developing the calibration phantom. It is shown that an aluminum phantom,

chosen for a similar X-ray attenuation to many geomaterials, can accurately correct for beam hardening observed in Poly[methylmethacrylate], which shares a close X-ray attenuation to that of water, and a wide range of meteoritic samples.

Applying this method of correction to a variety of meteoritic samples (Ozona, Grimsby, Gao-Guenie, and NWA 5480) we can begin to see the advantages of  $\mu$ CT to the study of geological samples.  $\mu$ CT is able to produce volumetric images of high resolution (20 – 50  $\mu\text{m}/\text{voxel}$ ) in highly weathered and therefore fine-grained samples such as Ozona, while it is still able to provide quantitative information about this sample. Utilizing a system of increased resolution (compared to the other samples examined) 3D images were produced of very small samples of the Grimsby meteorite, encased in epoxy mounts for SEM and EPMA work. Although the images were of high pixel resolution, the spatial resolution due to ring artifacts reduced the overall ability to analyze the data. It is nevertheless possible to separate metallic constituents (kamacite and taenite) and sulphide (troilite) from their surrounding silicate matrix, making metallic-plus-sulphide volume percentage measurements possible.

Within meteorites of high metallic content, such as Gao-Guenie, it is possible to segment high X-ray density materials (mostly kamacite and taenite, with some amounts of sulphides (Bourot-Denise et al., 1998)) from the surrounding matrix and chondrules, providing an 14.6% estimates of metal-sulphide content across the volume. This CT-derived metal-sulphide content is consistent with the 14% metal-sulphide content obtained by an area point-counting technique on the cut surface of the sample. In differentiated meteorites, with large grain size (as compared to voxel size), such as NWA 5480, it is possible to distinguish more subtle differences in the mineralogy, such as between olivine and orthopyroxene. This large grain size facilitates easier segmentation of the reconstruction volume. Using only a few points of reference on  $\mu$ XRD it is possible to cross reference the differences in radiodensity within the CT volume to mineralogy of the sample and allow for volumetric mineral content to be calculated.

## 4.2 Future Work

### 4.2.1 CT Calibration of Mineralogy

The successful validation of  $\mu$ CT for use in the assessment of volumetric and modal mineralogy, along with correction algorithms to reduce the inherent beam hardening associated with scanning dense objects will allow for numerous studies to take place. Although  $\mu$ CT is not inherently able to detect and report mineralogy, it is shown that closely associated silicate minerals, such as enstatite and forsterite, can be resolved. Volumetric information must satisfy the Nyquist sampling criteria, where in the sampling rate must be twice that of the spatial frequency, to provide adequate results. Careful collection and calibration of the reconstruction volume should provide the ability to discriminate and identify these minerals, and quantify their modal proportions, without the use of external sources for validation. This is obviously not possible for all minerals, as some have radiodensities that are too similar. Minerals that are adequately dissimilar in radiodensity (average radiodensity difference is about the noise of the volume) allow segmentation in the CT volume and should be able to be calibrated for (using individual protocols), enabling CT to be utilized as an identifying technique. It is important to note that this calibration and the limitations to discrimination are protocol (i.e. energy spectrum and intensity) dependent. Because minerals will absorb different amounts of photons across the energy spectrum, the contrast between the minerals can be enhanced or degraded, depending upon the energy used. Future studies should include the calibration of a variety of known type specimens within a range of dependable protocols. This can be extended to identifying the best scanning parameters to obtain the best contrast between the desired phases. Utilizing the NIST XCOM Database (Berger et al., 1998), it is possible to predict the energies that would be best phase separation.

### 4.2.2 Dual-Energy CT

One exciting field just emerging in medical imaging, is the use of two different source energies to scan the object. This is achieved by either a specialized CT scanner that has two sources and X-ray detectors working simultaneously (usually intended to reduce blur caused by the movement of living specimens), rapidly switching the X-ray source

between two energies, or by successive scanning of the same object at different protocols and co-locating and registering them (Panknin et al., 2009). As mentioned above, it is possible to determine X-ray spectra that will produce higher contrast between minerals that have similar X-ray attenuations at the same energy. By obtaining scans at two separate energies it becomes much easier to separate out the originally similar materials and provide a better differentiation of the volume for measurements (Johnson et al., 2007; Panknin et al., 2009).

### 4.2.3 Industrial Scanner Calibration

Industrial CT scanners provide X-ray spectra that are much higher in energy than the ones provided by biomedical scanners; >250 kVp compared to ~100 kVp, and therefore produce more of the highly penetrating photons. While industrial CT this produces images that show fewer artifacts caused by beam hardening, it still suffers from these artifacts due to the heterogeneous spectrum it uses. Newer systems, developed by Nikon Metrology, incorporate the ability to do beam hardening correction within their reconstruction software, however, they leave it up to the end user to calibrate the system. By utilizing the novel calibration phantom it is possible to provide correction on these machines, as well as any other industrial machine (provided there is user access to the projection data). Providing calibration and correction for systems of this type would allow for better data for the mineralogy of meteorites to be obtained.

### 4.3 References

- Baker, D., Mancini, L., Polacci, M., Higgins, M., Gualda, G., Hill, R., & Rivers, M. (2012). An introduction to the application of X-ray microtomography to the three-dimensional study of igneous rocks. *Lithos*, *148*, 262-276.
- Benedix, G., Ketcham, R., Wilson, L., McCoy, T., Bogard, D., Garrison, D., . . . Middleton, R. (2008). The formation and chronology of the PAT 91501 impact-melt L chondrite with vesicle-metal-sulfide assemblages. *Geochimica et Cosmochimica Acta*, *72*(9), 2417-2428.
- Berger, M., Hubbell, J., Seltzer, S., Chang, J., Coursey, J., Sukumar, R., . . . Olsen, K. (1998). XCOM: Photon cross sections database. *NIST Standard reference database*, *8*, 87-3597.
- Bourot-Denise, M., Wenmenga, U., & Christophe, M. (1998). The Guenie and Gao chondrites from Burkina Faso: Probably a single shower of stones. *Meteoritics & Planetary Science*, *33*(S4), A181-A182.
- Cunningham, K.J., & Sukop, M.C. (2011). Multiple technologies applied to characterization of the porosity and permeability of the Biscayne aquifer, Florida: U. S. Geological Survey.
- Cunningham, K.J., Sukop, M.C., Huang, H., Alvarez, P.F., Curran, H.A., Renken, R.A., & Dixon, J.F. (2009). Prominence of ichnologically influenced macroporosity in the karst Biscayne aquifer: Stratiform “super-K” zones. *Geological Society of America Bulletin*, *121*(1-2), 164-180.
- Ebel, D.S., & Rivers, M.L. (2007). Meteorite 3-D synchrotron microtomography: Methods and applications. *Meteoritics & Planetary Science*, *42*(9), 1627-1646.
- Ebel, D.S., Weisberg, M.K., Hertz, J., & Campbell, A.J. (2008). Shape, metal abundance, chemistry, and origin of chondrules in the Renazzo (CR) chondrite. *Meteoritics & Planetary Science*, *43*(10), 1725-1740.
- Friedrich, J.M., Wignarajah, D.P., Chaudhary, S., Rivers, M.L., Nehru, C., & Ebel, D.S. (2008). Three-dimensional petrography of metal phases in equilibrated L chondrites—Effects of shock loading and dynamic compaction. *Earth and Planetary Science Letters*, *275*(1), 172-180.
- Goergen, E.T., & Whitney, D.L. (2012). Corona networks as three-dimensional records of transport scale and pathways during metamorphism. *Geology*, *40*(2), 183-186.
- Hawkins, A., Selverstone, J., Brearley, A., Beane, R., Ketcham, R., & Carlson, W. (2007). Origin and mechanical significance of honeycomb garnet in high-pressure metasedimentary rocks from the Tauern Window, Eastern Alps. *Journal of Metamorphic Geology*, *25*(5), 565-583.

- Hirano, T., Funaki, M., Nagata, T., Taguchi, I., Hamada, H., Usami, K., & Hayakawa, K. (1990). *Observation of Allende and Antarctic meteorites by monochromatic X-ray CT based on synchrotron radiation*. Paper presented at the Proceedings of the NIPR Symposium on Antarctic meteorites.
- Hirose, T., & Hayman, N.W. (2008). Structure, permeability, and strength of a fault zone in the footwall of an oceanic core complex, the Central Dome of the Atlantis Massif, Mid-Atlantic Ridge, 30 N. *Journal of Structural Geology*, 30(8), 1060-1071.
- Johnson, T.R., Krauss, B., Sedlmair, M., Grasmuck, M., Bruder, H., Morhard, D., . . . Schmidt, B. (2007). Material differentiation by dual energy CT: initial experience. *European radiology*, 17(6), 1510-1517.
- Panknin, M.C., Ruehm, S., & Lell, M. (2009). Dual energy CT.

## Curriculum Vitae

**Name:** David Ryan Edey

**Post-secondary Education and Degrees:** The University of Western Ontario  
London, Ontario, Canada  
2005-2009 B.E.Sc. Mechanical Engineering

The University of Western Ontario  
London, Ontario, Canada  
2009-2010 B.Sc. Materials Science

The University of Western Ontario  
London, Ontario, Canada  
2010-2013 M.Sc. Geology

**Related Work Experience** Teaching Assistant  
The University of Western Ontario  
2010-2012

Research Assistant  
The University of Western Ontario  
X-ray Diffraction and Microdiffraction Laboratory  
09/2011-04/2012

### Publications:

Edey, D.R., Holdsworth, D., McCausland, P.J.A., and Flemming, R.L. (2013) Extended dynamic range micro-computed tomography of meteorites using a biomedical scanner. 44th Lunar and Planetary Science Conference, Abs. #2693. (Poster)

Flemming R.L., McCausland P.J.A., Izawa, M.R.M., Craig, M.A., Haring, M.M.M., Edey D.R. Shivak J.N., Kanhai J. Banerjee N.R., Osinski G.R. Holdsworth, D.W. Cloutis E., King P.L. (2011) Astromaterials I: Representative materials from across the solar system. Research Day, Centre for Advanced Materials and Biomaterials Research (CAMBR), June 23, 2011 (Poster).

Flemming R.L., McCausland P.J.A., Izawa, M.R.M., Craig, M.A., Edey D.R. Shivak J. N., Haring, M.M.M., Hainge, J.C., Banerjee, N.R., Osinski, G.R. (2011) Astromaterials II: Shock metamorphosed meteorites and terrestrial materials. Research Day, Centre for Advanced Materials and Biomaterials Research (CAMBR), June 23, 2011 (Poster)